

# Correcting estimations of copepod volume from 2-dimensional images

Cédric Dubois<sup>\*1</sup>, Jean-Olivier Irisson<sup>2</sup>, and Eric Debreuve<sup>1</sup>

<sup>1</sup>Université Côte d'Azur, CNRS, Inria, Équipe Morpheme, Laboratoire I3S,  
Sophia Antipolis, France. \*Corresponding author:  
[cedric.dubois@univ-cotedazur.fr](mailto:cedric.dubois@univ-cotedazur.fr)

<sup>2</sup>Sorbonne Université, CNRS, Équipe COMPLEX, Laboratoire LOV, Institut IMEV,  
Villefranche-sur-mer, France.

**Keywords**—Zooplankton, Volume, Biomass, Copepod, Geometrical model,  
*in situ* imaging.

## Abstract

Accurate plankton biomass estimations are essential to study marine ecological processes and biogeochemical cycles. This is particularly true for copepods, which dominate mesozooplankton. Such estimations can efficiently be computed from organism volume estimated from images. However, imaging devices only provide 2D projections of 3D objects. The classical procedures to retrieve volumes, based on the Equivalent Spherical Diameter (ESD) or the best-fitting ellipse, are biased. Here, we present a method to correct these biases. First a new method aims to measure body area and fit an ellipse. Then, the body of copepods is modeled as an ellipsoid whose 2D silhouette is mathematically derived. Samples of copepod bodies are simulated with realistic shapes/sizes and random orientations. Their total volume is estimated from their silhouettes using the two classical methods and a correction factor is computed, relative to the known, total, volume. On real data, individual orientations and volumes are unknown but the correction factor still holds for the total volume of a large number of organisms. The correction is around -20% for the ESD method and +10% for the ellipse method. When applied to a database of  $\sim$ 150,000 images of copepods captured by the Underwater Vision Profiler, the corrections decreased the gap between the two methods by a factor of 54. Additionally, the same procedure is used to evaluate the consequence of the bias in the estimation of individual volumes on the slopes of Normalised Biovolume Size Spectra and show that they are, fortunately, not sensitive to the bias.

## Introduction

Plankton forms an extremely diverse community (de Vargas et al., 2015) and its members are keystone components of Earth's biosphere. First, photosynthetic plankton is responsible for about half of the fixation of carbon dioxide from the atmosphere and therefore produces an equally large amount of dioxygen (Behrenfeld et al., 2001). The death and excretion of planktonic organisms result in massive amounts of carbon being sequestered to the seabed in the form of "marine snow"; this "biological carbon pump" is therefore an important contributor to the regulation of climate (Volk and Hoffert, 1985). Plankton is also a critical component of many marine food webs: it directly supports some of the largest fisheries on earth, off the coast of Chile for example (Thiel et al., 2007), and some emblematic species such as corals. Finally, because plankton simply drifts, it cannot escape the conditions of the water mass it is embed-

ded in. This makes planktonic organisms very sensitive to environmental change. Therefore, the contribution of plankton to the important processes described above will be influenced by the changes in Earth's climate (Hays et al., 2005).

To quantify these roles of plankton and their possible change in time, accurate estimations of its biomass are needed. Major efforts have been made in that direction, to aggregate estimates from various techniques in pan-oceanic databases (Buitenhuis et al., 2013; Moriarty and O'Brien, 2013). These assessments are unfortunately fraught with uncertainties due, for example, to the difficulty of sampling plankton in open and deep seas, resulting in an uneven coverage, and to the differences between sampling techniques. Recently, the use of quantitative imaging instruments, i.e. automated cameras that take pictures at high frequency in a controlled manner that allows the computation of concentrations, have been highlighted as a one promising avenue for the estimation of plankton biomass and biodiversity at global scale (Lombard et al., 2019). However, most of these instruments take two-dimensional pictures, which reduce the organism to its projection on the imaged plane. The volume of organisms is estimated from this imperfect representation, mostly using two classic approaches detailed below (a spherical equivalent or an ellipsoidal approximation) and then converted to carbon biomass through a factor (their carbon density). For any organism that is not perfectly spherical, both approaches induce an error in the volume and therefore the biomass, that has been neglected so far.

Several of these quantitative imaging instruments target mesozooplankton (organisms between  $\sim 200 \mu\text{m}$  and  $\sim 2 \text{ mm}$  in size), which are major contributors to biogeochemical fluxes in the ocean (Buitenhuis et al., 2006). Within mesozooplankton, copepods represent about 85% of organisms (Longhurst, 2007) and contribute largely to the carbon flux by grazing on smaller plankton, producing fecal pellets and dead carcasses that sink. The intensity of that flux is proportional to the biomass of organisms, particularly those present in the surface, mixed layer (Buitenhuis et al., 2006). Because copepods are not spherical but rather ellipsoidal (Fig. 1), the estimation of their volume by imaging instruments is affected by the aforementioned projection error.

The purpose of the present work is to quantify the error in the estimation of the total volume of copepods from a collection of two dimensional images and to propose a correction of this estimation. This error can potentially change current estimations of carbon biomass in those organisms significantly, and its relationship with the carbon flux they generate. Both are important parameters of global biogeochemical models (Buitenhuis et al.,

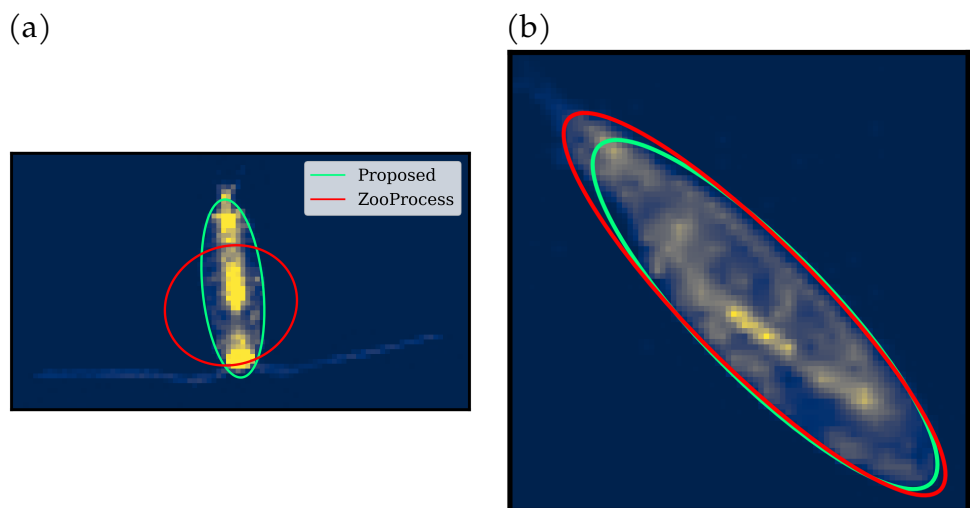


**Figure 1:** Examples images of copepods and theirs ellipse fits: (a) top or bottom view, (b) side view. On these projections, the bodies of copepods can be well approximated by ellipses, which we assume to be ellipsoids in 3 dimensions (see Supporting Information S1). Ellipse fits on copepod images are obtained by ZooProcess (Gorsky et al., 2010) in red, affected by the antennae, and our method in green, that fits the prosome of the copepod better.

2006). We start by reviewing the two standard methods to estimate the volume of planktonic objects from their two-dimensional projection and detail the magnitude of errors they induce. We then present our correction method, followed by an application to a global data set of copepod images collected by the Underwater Vision Profiler (Picheral et al., 2010). Finally we conclude and present perspectives for this work.

## Standard volume estimations

To safely infer a volume in three dimensions from a shape projected in two dimensions, the following assumptions are made:

- The distance between imaged objects and the camera is the same for all objects (or differences are negligible).
- One of the two following statements is true.
  - The size of the object is negligible compared to its distance from the camera. Hence, even if the camera has a perspective acquisition geometry, it can be approximated well enough by a parallel one.
  - The acquisition system follows a line scanner principle (then, its acquisition geometry is intrinsically parallel);

With these hypotheses, the imaging process can be schematically represented as in Fig. 2. All *in situ* plankton imagers presented in (Lombard et al., 2019) satisfy these conditions.

Then, an hypothesis on the three dimensional shape of the object has to be made. Two standard approaches exist: a spherical equivalent and an ellipsoidal hypothesis.

### Using a spherical equivalent ( $\mathcal{M}_{\text{ESD}}$ )

There is a unique disk with the same area  $A$  as the organism's projected silhouette (the silhouette of the organism as observed on the image), and its diameter is  $\text{ESD} = 2\sqrt{\frac{A}{\pi}}$ . The Equivalent Spherical Diameter estimation method ( $\mathcal{M}_{\text{ESD}}$ ) makes the assumption that the volume of the organism can be approximated by the volume of the sphere of diameter ESD, that is

$$V_{\text{ESD}} = \frac{4}{3}\pi\left(\frac{\text{ESD}}{2}\right)^3. \quad (1)$$

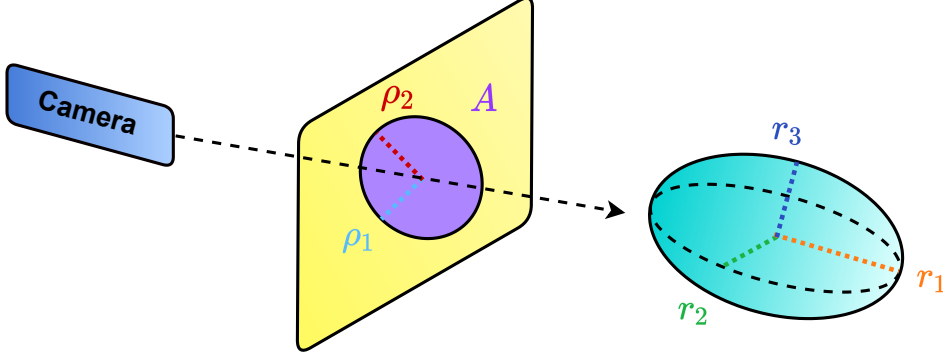


**Figure 2:** Representation of the geometrical setup of the imaging, with some notations:  $r_1$ ,  $r_2$ , and  $r_3$  the true semi-axes of an ellipsoidal object, with  $r_1 \geq r_2 \geq r_3$  by convention;  $\rho_1$ ,  $\rho_2$  the semi-axes of the projected ellipse, with  $\rho_1 \geq \rho_2$  by convention;  $A$  the area of the projected shape.

If the organisms were indeed spherical and the 3-D-to-2-D acquisition system performs a parallel projection, then  $V_{\text{ESD}}$  would be the exact volume.

For ellipsoidal objects, like copepods, the projection silhouette is an ellipse of semi-axes  $\rho_1$  and  $\rho_2$ , with  $\rho_1 \geq \rho_2$  by convention (see Fig. 2). Its area is equal to  $\pi\rho_1\rho_2$ . Therefore, the equivalent diameter is  $\text{ESD} = 2\sqrt{\rho_1\rho_2}$ . In that case, the error of the  $\mathcal{M}_{\text{ESD}}$  estimation can range from large underestimation to even larger overestimation, when the copepod is elongated in the direction of the optical axis (Fig. 3).

### Using a best-fitting ellipse ( $\mathcal{M}_{\text{ELL}}$ )

A common alternative to  $\mathcal{M}_{\text{ESD}}$  is to fit an ellipse shape on the projection and construct an ellipsoid in three dimensions ( $\mathcal{M}_{\text{ELL}}$ ). It should be more appropriate for objects of ellipsoidal shape, such as copepods (assuming the antennae and urosome are thin/small enough for their influence on the volume to be negligible). It proceeds as follows: (i) an ellipse is fitted on the object silhouette, defining two semi-axes:  $\rho_1$  and  $\rho_2$  (Fig. 2), (ii) the smallest semi-axis of the fitted ellipse ( $\rho_2$ ) is duplicated to form the triplet of semi-axes of an ellipsoid, (iii) the volume is computed as

$$V_{\text{ELL}} = \frac{4}{3}\pi\rho_1\rho_2^2. \quad (2)$$

Despite the fact that the estimation of the silhouette shape is more appropriate than with  $\mathcal{M}_{\text{ESD}}$ , it still leads to errors due to the projection from 3D to 2D (Fig. 3). We can remark that, within this ellipsoid model frame-

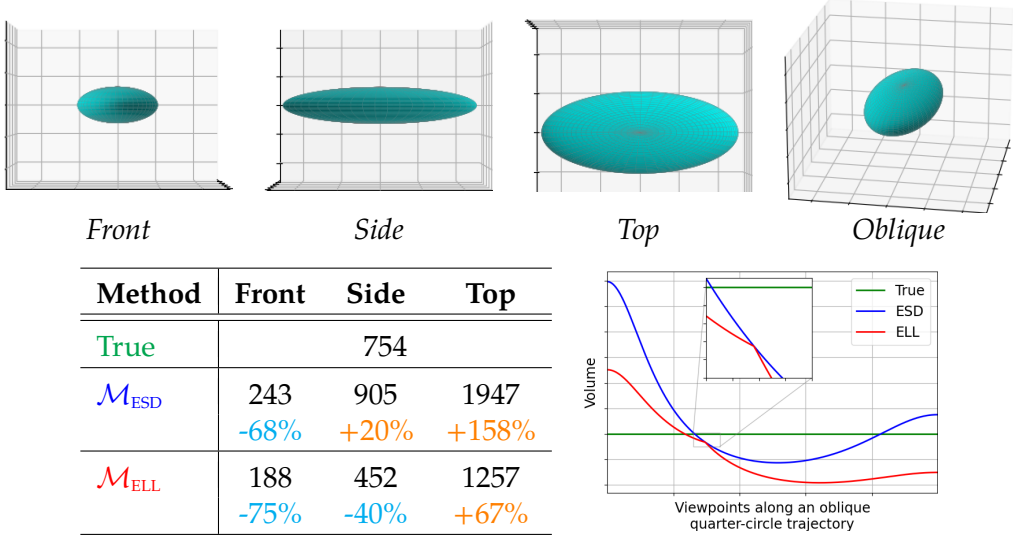


**Figure 3:** Examples of volume estimations and errors made by  $\mathcal{M}_{\text{ESD}}$  and  $\mathcal{M}_{\text{ELL}}$  for an ellipsoid  $E$  with  $(r_1, r_2, r_3) = (12, 5, 3)$  (see Fig. 2 for the definition of  $r_i$ ). The first row displays the simulated ellipse from various viewing angles. The table gives, in black, the rounded values of the volume for each method and, in colour, the percentage of under/over estimation compared to the true value, which is computed from the  $r_i$ s. The individual volume estimation error is invariant to scaling (see Supporting Information S2), therefore any ellipsoid respecting  $r_2/r_1 = 5/12$  and  $r_3/r_1 = 3/12$  would lead to the same error percentages. The lower right plot shows the volume computed with each method for viewpoints regularly sampled along an arc turning around the ellipsoid; note that the  $\mathcal{M}_{\text{ESD}}$  estimation is always greater than or equal to the  $\mathcal{M}_{\text{ELL}}$  one.

work,  $V_{\text{ELL}}$  is always lower than or equal to  $V_{\text{ESD}}$ . Indeed, we assume  $\rho_1 \geq \rho_2$ , therefore

$$\begin{aligned} & \sqrt{\rho_1 \rho_2} \geq \rho_2 \\ \Leftrightarrow & \sqrt{\rho_1 \rho_2}^3 \geq \rho_1 \rho_2^2 \\ \Leftrightarrow & V_{\text{ESD}} \geq V_{\text{ELL}} \end{aligned}$$

with equality when the projection silhouette is a circle.

## Proposed method

Instead of proposing a novel volume estimation method, our approach was to study the errors made by the standard methods  $\mathcal{M}_{\text{ESD}}$  or  $\mathcal{M}_{\text{ELL}}$  in order to propose a procedure to compensate for these errors. Thus, the figures of past studies could be re-interpreted in light of the proposed corrections and marine ecologists could apply these corrections to future studies, sticking to their standard estimation method of choice.

However, we noticed that copepod antennae, when visible, can affect, sometimes dramatically, the measurement of the projected area of their prosome (which constitutes the bulk of their volume) or the fitting of an ellipse to their silhouette (Fig. 1). Therefore, as a preliminary step, we propose area estimation and ellipse fitting approaches tailored to copepods, to mitigate that phenomenon. The area estimation is based on a form of mathematical morphology opening that first performs an erosion to discard the antennae and then a dilation to recover the area of the copepod body. The proposed ellipse fitting method relies on the same operations for discarding the antennae and ensuring a better fit of the ellipse (see Supporting Information S3 for details).

## Principle for correction of total volume

To derive the correction to apply to a volume estimated with  $\mathcal{M}_{\text{ESD}}$  or  $\mathcal{M}_{\text{ELL}}$ , we model the body of a copepod by an ellipsoid (i.e. in three dimensions), study how an ellipsoid projects onto a plane, estimate the volume from its projection using  $\mathcal{M}_{\text{ESD}}$  and  $\mathcal{M}_{\text{ELL}}$ , and compare it with the known, ground-truth volume of the ellipsoid model. This process is performed on many ellipsoids, projected at many angles, and the correction is computed on the overall, total, volume because it is impossible to retrieve the projection angle and 3-D shape from only the projected silhouette of an object in a single imaging plane.

This process amounts to (i) neglecting the volume of the antennae and urosome, which is an assumption implicitly made by the existing methods; (ii) not considering acquisition phenomena such as optical response and electronic noise, hence reducing the imaging process to the 3-D to 2-D projection onto the camera sensor plane, because those processes are not general (i.e. camera-dependent) and most often not characterised for plankton cameras; (iii) considering the acquisition projection parallel, which is most often the case in our applicative context (see section Section “Standard volume estimations”) and simplifies the theoretical study (some supplementary materials still consider the more general perspective case, before applying it to the parallel case).

## Silhouette of a projected ellipsoid

An ellipsoid centered on the origin is composed of the ensemble of 3-D points  $x$  verifying

$$x^\top M x = 1 \quad (3)$$

where  $M$  is a real, symmetric, positive definite,  $3 \times 3$ -matrix whose elements are denoted by  $m_{ij}$ . The volume of the ellipsoid is defined by

$$V = \frac{4}{3} \frac{\pi}{\sqrt{\det(M)}}. \quad (4)$$

Matrix  $M$  encodes the overall size, shape (semi-axes ratios) and orientation of the ellipsoid. It can be written using a block matrix notation

$$M = \left[ \begin{array}{c|c} M_{11} & M_{21}^\top \\ \hline M_{21} & m_{33} \end{array} \right] \quad (5)$$

where  $m_{33}$  is a scalar (the dimensions of the other terms follow). If the ellipsoid is aligned on the axes of the coordinate system, then its form is

$$M = \begin{bmatrix} 1/r_1^2 & 0 & 0 \\ 0 & 1/r_2^2 & 0 \\ 0 & 0 & 1/r_3^2 \end{bmatrix} \quad (6)$$

where the  $r_i$ 's are the semi-axes.

In Supporting Information S1, it is shown that the silhouette of the parallel projection of an ellipsoid is an ellipse, the two semi-axes of which are defined by

$$\rho_i = \sqrt{\frac{m_{33}}{\lambda_i}}, i \in \{1, 2\} \quad (7)$$

where

$$\lambda_i = \left( \text{tr}(P) + \sigma_i \sqrt{\Delta} \right) / 2, \quad (8)$$

$$P = m_{33} M_{11} - M_{21}^T M_{21}, \quad (9)$$

$$|\sigma_i| = 1 \text{ and } \sigma_1 \sigma_2 = -1, \quad (10)$$

$$\Delta = \text{tr}(P)^2 - 4 \det(P) \quad (11)$$

where  $\text{tr}(P)$  is the trace of  $P$ ,  $\det(P)$  is its determinant, and the  $\sigma_i$ 's are chosen so that  $\rho_1 \geq \rho_2$ .

From these developments, we therefore have analytical (i.e. exact) definitions of an ellipsoid, its volume, its projection as an ellipse, the semi-axes and area of this projected ellipse.

## Simulation of copepod bodies

By generating random ellipsoids that realistically represent copepod body shapes, observations of their projections on images can be simulated exactly, since the  $\rho_i$ 's are functions of  $M$  (i.e. the semi-axes of the observed elliptical silhouette depends on the ellipsoid size, shape, and orientation).

The simplest choice to generate ellipsoids would be to draw the semi-axes from independent uniform distributions within appropriate ranges — valid ranges can be found in the literature (e.g. Conway, 2012) — and the orientation angle from an unconstrained uniform distribution. However, those parameters should ideally be adapted to the data set at hand, since copepod sizes, shapes, and acquisition viewpoints (or orientations) are related to environmental and imaging conditions. In the following, we propose a way to generate ellipsoids that follow a realistic, parametric copepod body model.

To generate random ellipsoids, one can directly generate random matrices  $M$  as defined in section Section “Silhouette of a projected ellipsoid”. Alternatively, random axis-aligned ellipsoids can be generated, which are then randomly rotated. The advantage of this later procedure is that constraints are more easily imposed to create copepod bodies with realistic proportions.

Following Eq. (6), axis-aligned ellipsoids are defined by the three semi-axes  $r_1$ ,  $r_2$ , and  $r_3$ . Since ellipsoids will be randomly rotated next, these values can be chosen such that  $r_1 \geq r_2 \geq r_3$  without loss of generality. To generate random values of  $r_1$ ,  $r_2$ , and  $r_3$ , we need to define one Probability Density Function (PDF, or “distribution”) per  $r_i$ . These PDFs must be defined in accordance with the reality of copepod body shapes, either

generically (e.g., according to the literature) or from the data at hand. Generating an ellipsoid then amounts to drawing one random semi-axis per PDF. If the semi-axes respect the ordering condition, then the ellipsoid is validated; otherwise, it is discarded, and a new round of random drawing must be performed. As such, the random process is of dimension three ( $r_1, r_2, r_3$ ) with two conditions ( $r_1 \geq r_2$  and  $r_2 \geq r_3$ ).

Fortunately, the process can be simplified by noting that the error made by the  $\mathcal{M}_{\text{ESD}}$  or the  $\mathcal{M}_{\text{ELL}}$  method on the total volume estimation is (almost) invariant to scaling (see Supporting Information S2). In other words, the error computed from  $N$  ellipsoids defined by  $(r_{1,n}, r_{2,n}, r_{3,n}), n \in [1..N]$  is (almost) equal to the error computed by the same ellipsoids each scaled by a constant  $\alpha_n$  strictly positive (i.e. defined by  $(r_{1,n}/\alpha_n, r_{2,n}/\alpha_n, r_{3,n}/\alpha_n)$ ). Choosing  $\alpha_n = r_{1,n}$  amounts to normalizing the ellipsoids so that their largest semi-axis is equal to one. Thus, the random process becomes two-dimensional (defined only by the axes ratios  $r_2/r_1$  and  $r_3/r_1$ ) with only one condition ( $r_2/r_1 \geq r_3/r_1$ ); the three, per-axis PDFs are replaced by two axes-ratio PDFs. This has two nice consequences: a statistical one and a practical one. Statistically speaking, to describe a random process through simulation, one needs “exponentially” more samples as the dimension increases (this is known as the curse of dimensionality). The number of samples,  $N$ , is limited by computational constraints; thus, reducing the dimension provides a higher quality description for the same  $N$ . Practically speaking, the shift from drawing semi-axes to drawing semi-axes *ratios* means that the proposed method only depends on the *shape* of copepods (prosome height over prosome length and prosome width over prosome length), not on their overall size, which can be considered more general (size varies across regions) and more stable.

The remaining question is how to define the PDFs of the semi-axes ratios  $r_2/r_1$  and  $r_3/r_1$ ? As for the per-axis PDFs, two reasonable options are literature-based and data-based. The literature may provide enough details to choose a PDF family (e.g., Gaussian) and set the parameters for each ratio (e.g., mean and variance for Gaussian). Alternatively, the ratios can be measured on physical samples or on images in which the copepods are seen from side ( $r_2/r_1$  ratio) and from the top or bottom ( $r_3/r_1$  ratio). Then, the required PDFs can be fitted on these measurements in a parametric (e.g., Gaussian, Beta, Gaussian mixture (Redner and Walker, 1984)) or non-parametric way (e.g., Kernel Density Estimation, KDE (Parzen, 1962; Scott, 1979)).

Finally, these ellipsoids, generated to match copepod body shapes, must be rotated to simulate a random acquisition viewpoint. In the absence of a strong a priori on the orientation of copepods relative to the camera, these

rotations can simply be uniformly random, in all directions. But the procedure can easily be adapted to generate rotations favoring preferred orientations.

## Corrected total volume

Once a set of  $N$  random ellipsoids with realistic proportions and various orientations is generated, their projection silhouettes are computed following Eq. (7), their volumes are estimated using  $\mathcal{M}_{\text{ESD}}$  (from the area of the silhouettes) and  $\mathcal{M}_{\text{ELL}}$  (from the semi-axes of the silhouettes), and the error between the total, true, volume of all ellipsoids and the sum of the estimated volumes is computed as

$$\mathcal{T}_* = \frac{\sum_{n=1}^N V_*^n}{\sum_{n=1}^N V^n} = \frac{W_*}{W} \quad (12)$$

where the  $V^n$ s are the true volumes of the generated ellipsoids and the  $V_*^n$ s are the corresponding estimated volumes by method “\*” (ESD or ELL). Therefore,  $W$  is the true total volume of all ellipsoids in the simulation and  $W_*$  is the estimated total volume.

Once  $\mathcal{T}_*$  has been estimated from simulated ellipsoids, it can be used to correct the total volume estimated from  $P$  actual images of copepods as follows

$$W_*^c = \frac{\sum_{p=1}^P V_*^p}{\mathcal{T}_*} = \frac{W_*^u}{\mathcal{T}_*} \quad (13)$$

where  $V_*^p$  is the set of volumes estimated from the acquired images by method “\*”,  $W_*^u$  is their total, and  $W_*^c$  is the corrected total estimated volume.

Note that the proposed correction formula in Eq. (13) provides no objective element to prefer the  $\mathcal{M}_{\text{ESD}}$  method over the  $\mathcal{M}_{\text{ELL}}$  method, or vice versa. Indeed, the respective correction factors theoretically allow to perfectly retrieve the true total volume. In practice though, the  $\mathcal{M}_{\text{ESD}}$  method might be a better option since the area measurement it relies on is more robust (i.e., less sensitive to acquisition noise and grayscale variations) than the ellipse fit performed in the  $\mathcal{M}_{\text{ELL}}$  method.

An algorithmic description of the proposed method is given in Supporting Information S4. A Python implementation is available at:  
<https://gitlab.inria.fr/cedubois/Copepod-Volume-Correction>.

## Extension to size spectra

Plankton images are often used to estimate the size of organisms and, in particular, to compute Normalised Biomass (or Biovolume) Size Spectra (NBSS). Indeed, the slope of these spectra is a proxy for the efficacy of the energy transfer from small to large organisms within an ecosystem (Sprules and Barth, 2016). An NBSS obviously depends on the measurement of the size of the organisms it encompasses and, therefore, its slope may be affected by the error in the size estimation due to the 3-D to 2-D projection. We will test this through a simulation procedure, similar to the one described above, and compare the slope value computed from the volumes of randomly generated ellipsoids (considered as the true value) to that derived from estimations of volume from their projections using  $\mathcal{M}_{\text{ESD}}$  and  $\mathcal{M}_{\text{ELL}}$ .

Since the NBSS depends on absolute sizes, the simulator based on standardised ellipsoids, defined by  $r_1 = 1$  and two semi-axes ratios, must be reverted to use directly  $r_1$ ,  $r_2$ , and  $r_3$ , although this is a less favorable statistical context (see section Section “Simulation of copepod bodies”). As mentioned previously, the distributions of  $r_1$ ,  $r_2$ , and  $r_3$  can be defined from the literature or estimated from measurements. Then the constructed ellipsoids must be rotated, either uniformly or along a preferred orientation.

## Experimental results

### Data set

We applied the proposed method to a collection of 158,487 copepod images from the Underwater Vision Profiler 5 (UVP5) (Picheral et al., 2010). Images are grayscale, with a pixel size varying from 0.086 to 0.174 mm depending on the generation and configuration of the UVP5. These pixel sizes are used to rescale all measurements to millimeters before computation. For each image, the area measurement and the ellipse fit had been performed with the original image analysis software (ZooProcess). They were carried out again following the new image processing method described in Supporting Information S3. When the newly estimated volume from either  $\mathcal{M}_{\text{ESD}}$  or  $\mathcal{M}_{\text{ELL}}$  was below  $0.1 \text{ mm}^3$ , the copepod silhouette detection was considered erroneous and the image was excluded from the data set. Images of partially cropped copepods (i.e. with a part of the body outside of the image) were also excluded, since they would bias the estimation of the area and the semi-axes. Around 2,500 images were excluded (<2%

of the data set), leaving 155,936 copepod images for the following.

## Total volume

As explained above, simulating copepod bodies for a correction of their overall volume requires PDFs for the two semi-axes ratios  $r_2/r_1$  and  $r_3/r_1$  and a rotation angle. We assumed uniform random orientation of copepods in the water column, since the data set is large, covers different depths and locations on the globe, and we do not know of any justification for a preferred orientation relative to the camera. The procedure for the axes-ratio is described below.

### Estimating shape parameters

The axes ratios were measured on 295 images in which copepods were seen from the side and 265 images in which they were seen from the top or bottom. To build these samples, operators manually selected images in which the orientation of the copepod was clear, while constraining the selection to obtain distributions in latitude similar to those of the whole data set and distributions in length similar between the side and top/bottom samples (see Supporting Information S5). The constraint on latitude was meant to avoid biasing the samples towards a particular environment, since copepod morphology varies latitudinally. The constraint in prosome length should ideally have been checked against the whole data set, to avoid estimating the axes ratios on biases samples of the  $\sim 150k$  images. However, the true prosome length, or  $2 \times r_1$  in the 3-D ellipsoid, is unknown; only  $2 \times \rho_1$ , the major axis of the projected ellipse, can be estimated. While  $r_1 \simeq \rho_1$  in the side and top/bottom views,  $r_1 > \rho_1$  in any other view, so only the distribution of  $\rho_1$  in the side and top/bottom views can be compared. The PDFs for  $r_2/r_1$  and  $r_3/r_1$  were then estimated from the measurements using a KDE with a Gaussian kernel of optimal width (Scott, 1979) (see Fig. 4).

### Computing the correction factor

Once the axes ratio PDFs were fitted to the manually selected data, we used the simulation procedure presented above to compute the error in the estimation of volume  $T_*$ , for both methods. We generated  $10^8$  ellipsoids in order to cover the shape and orientation parameters space with a high enough resolution (see Supporting Information S7 for a study of the influence of the number of ellipsoids). Using Eq. (12), we obtained  $T_{\text{ESD}} =$

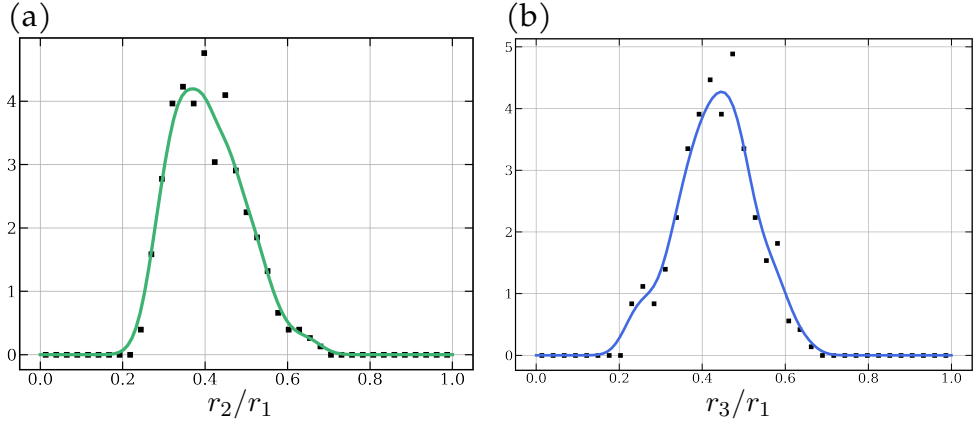


**Figure 4:** Distributions of  $r_2/r_1$  (a) and  $r_3/r_1$  (b) fitted on our data set. The markers are the normalized histograms of the samples and the solid lines are the Gaussian Kernel Density Estimates.

122% and  $\mathcal{T}_{\text{ELL}} = 87\%$ . In other words, on average,  $\mathcal{M}_{\text{ESD}}$  overestimated the true volume by 22% while  $\mathcal{M}_{\text{ELL}}$  underestimated it by 13%.

Let us note that, as expected,  $\mathcal{T}_{\text{ESD}}$  is higher than  $\mathcal{T}_{\text{ELL}}$ , since we showed that the  $\mathcal{M}_{\text{ESD}}$  volume is always greater than or equal to the  $\mathcal{M}_{\text{ELL}}$  volume. Also, the correction factors are then simply computed as  $1/\mathcal{T}_{\text{ESD}}$  and  $1/\mathcal{T}_{\text{ELL}}$ .

These correction factors were obtained under the assumption that they were invariant to ellipsoid scaling (Supporting Information S2). To verify that this is reasonable, we performed a similar simulation in the (less convenient) three parameters space  $(r_1, r_2, r_3)$ , also using  $10^8$  ellipsoids. For that purpose, the distributions of  $r_1$ ,  $r_2$ , and  $r_3$  were needed. The generation of these distributions is detailed in the section regarding NBSS, below. In this framework, the errors in volume estimation were  $\mathcal{T}_{\text{ESD}}^{3D} = 129\%$ , so +6% compared to  $\mathcal{T}_{\text{ESD}}$ , and  $\mathcal{T}_{\text{ELL}}^{3D} = 84\%$ , -3% compared to  $\mathcal{T}_{\text{ELL}}$ . Part of this discrepancy may come from a coarser coverage of the parameters space in this three parameters case. It can be concluded that, indeed, the assumption of invariance to ellipsoid scaling made in the proposed method is reasonable.

### Estimating and correcting the total volume

We estimated the total volume of the  $\sim 150k$  copepods in our data set using various approaches: the  $\mathcal{M}_{\text{ESD}}$  or  $\mathcal{M}_{\text{ELL}}$  method, as computed originally by ZooProcess (*ZP*) or using our improved method (Supporting Information S3), and with or without the corrections using the factors defined above. This is a total of eight estimations, presented in Fig. 5.

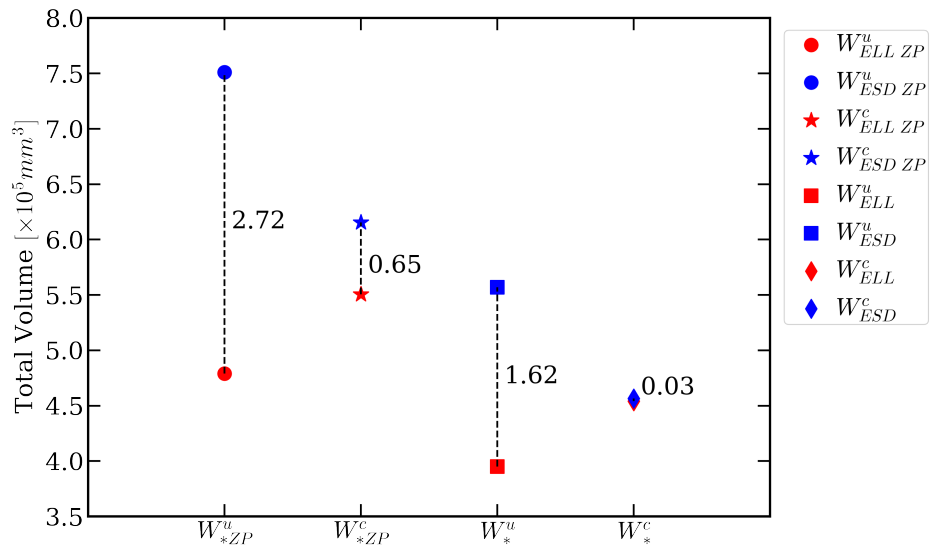


**Figure 5:** Total volume estimated by  $\mathcal{M}_{\text{ESD}}$  (blue) or  $\mathcal{M}_{\text{ELL}}$  (red) obtained by ZooProcess ( $ZP$ ) and our improved measures, uncorrected ( $W^u$ ) or corrected ( $W^c$ ). The discrepancies between the methods are highlighted by dashed lines and annotated by the corresponding absolute differences. The proposed correction drastically reduces these discrepancies, although there is no way to tell which result would be more realistic between  $\mathcal{M}_{\text{ESD}}$  or  $\mathcal{M}_{\text{ELL}}$  before correction.

In theory (i.e. copepods are ellipsoids, the imaging system has perfect lenses and infinite resolution, surface measurements and ellipse fits are exact, the simulation parameters match the reality, an infinite number of samples are generated), we should obtain the same total volume estimations from  $\mathcal{M}_{\text{ESD}}$  and  $\mathcal{M}_{\text{ELL}}$  after correction. Naturally, this is not the case in practice but we can assess the effectiveness of the proposed volume correction by checking how the discrepancy between the  $\mathcal{M}_{\text{ESD}}$  or  $\mathcal{M}_{\text{ELL}}$  estimations decreases after applying the correction. This gap is divided by 4 when using the ZooProcess measurements and by 54 when using the improved versions. The fact that the corrected volumes ( $W_{\text{ESD}}^c$  and  $W_{\text{ELL}}^c$ ) seem to converge is no proof that either one is the truth, but it at least suggests that the proposed correction method brings a significant improvement.

The impact of the improved area and ellipse measurement can also be gauged in the same way. The discrepancy is divided by 2 when comparing  $W_{*ZP}^u$  and  $W_*^u$ , and by 22 when comparing the corrected versions,  $W_{*ZP}^c$  and  $W_*^c$ . This illustrates that some accuracy can also be gained in these image processing steps. Overall, if we compare the current state of the art (uncorrected total volumes obtained using classical image processing in ZooProcess) and the corrected total volumes obtained using improved image processing, the discrepancy is divided by 91, bringing the  $\mathcal{M}_{\text{ESD}}$  and  $\mathcal{M}_{\text{ELL}}$  estimations very close to each other.

## Normalized Biovolume Size Spectrum (NBSS)

### Estimating shape parameters

As explained above, NBSS relies on absolute volumes and the distributions of the three semi-axes ( $r_1$ ,  $r_2$ , and  $r_3$ ) have to be estimated. They could have been estimated directly on the 295 + 265 samples used to estimate the distributions of ratios above. However, the distribution of  $r_1$  for the 295 copepods viewed from the side shows a bias towards larger sizes, because it is difficult to tell whether a copepod is indeed viewed from its side when it is small (see Supporting Information S5). This bias has limited influence on the estimation of the distributions of the ratios,  $r_2/r_1$  and  $r_3/r_1$ , since the both relationships  $r_1$  vs.  $r_2$  and  $r_1$  vs.  $r_3$  are fairly linear (Fig. 6). Therefore, it was safely dismissed for the correction of the total volume, above, which relied solely on those ratios. This is not possible anymore. Instead, we build the distribution of  $r_1$  from the ~150k measurements of  $\rho_1$ , its projection in the 2D plane, which can be seen as an underestimated version of  $r_1$ . To correct for the underestimation, we multiply the values of  $\rho_1$  by a constant,  $C_r \simeq 1.12$ . This value is computed from the median  $r_1/\rho_1$  ra-

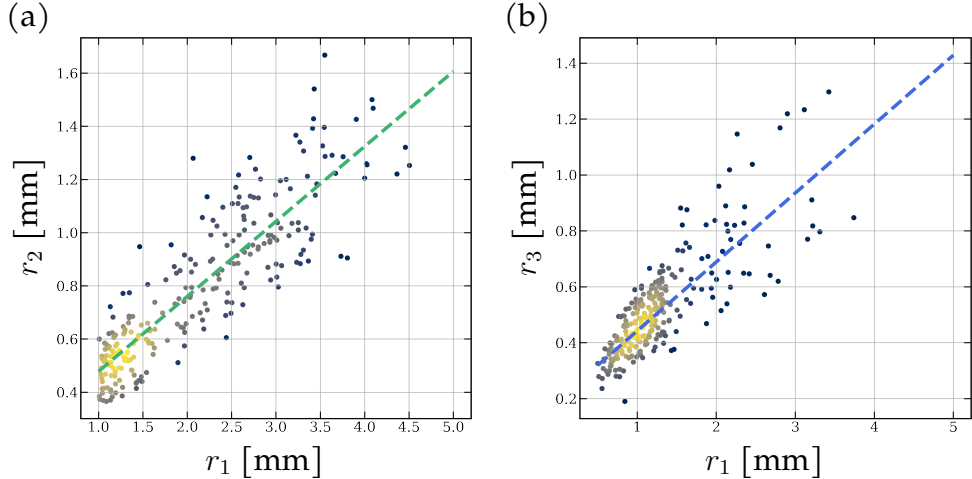


**Figure 6:** (a) Relationship between  $r_2$  and  $r_1$  from 254 copepods seen from the side, for  $r_1 > 1$  mm. (b) Relationship between  $r_3$  and  $r_1$  from the 173 copepods seen from the top or bottom, for  $r_1 > 1$  mm. The colored dashed line are linear regressions fits, significant in both cases ( $p < 0.01$ ,  $R^2 = 88\%$  for (a) and  $R^2 = 75\%$  for (b)). The color scale of points represents the density of samples.

tios observed in the previous simulation of the  $10^8$  ellipsoids projected as ellipses.

For a smoother distribution of  $r_1$ , a fourth-order polynomial is fitted on the log-distribution in the range  $\sim [1.5, 5.5]$  mm, and extrapolated outside of this interval (Fig. 7). The lower limit (1.5 mm) corresponds to the start of the continuously decreasing section; before this, copepods are difficult to identify on UVP5 images and are undersampled. The higher limit (5.5 mm) is the point beyond which the density of samples is too low, making the distribution very noisy.

The values of  $r_2$  and  $r_3$  are then deduced from the value of  $r_1$ , following Fig. 6, were it can be seen that (i)  $r_2$  and  $r_3$  increase linearly with  $r_1$ , (ii) the variance around the linear fit also increases with  $r_1$ .

Finally, the values of  $r_i$ s are generated as follows: a value of  $r_1$  is drawn from its estimated distribution (Fig. 7), then values of  $r_2$  and  $r_3$  are drawn from a normal distribution with mean ( $\mu$ ) and standard deviation ( $\sigma$ ) computed from  $r_1$ :  $\mu_2 = 0.3 \times r_1 + 0.18$ ,  $\mu_3 = 0.21 \times r_1 + 0.26$ ,  $\sigma = 0.05 \times r_1$  (from the fits on Fig. 6). Only samples respecting the condition  $r_1 \geq r_2 \geq r_3$  are kept.

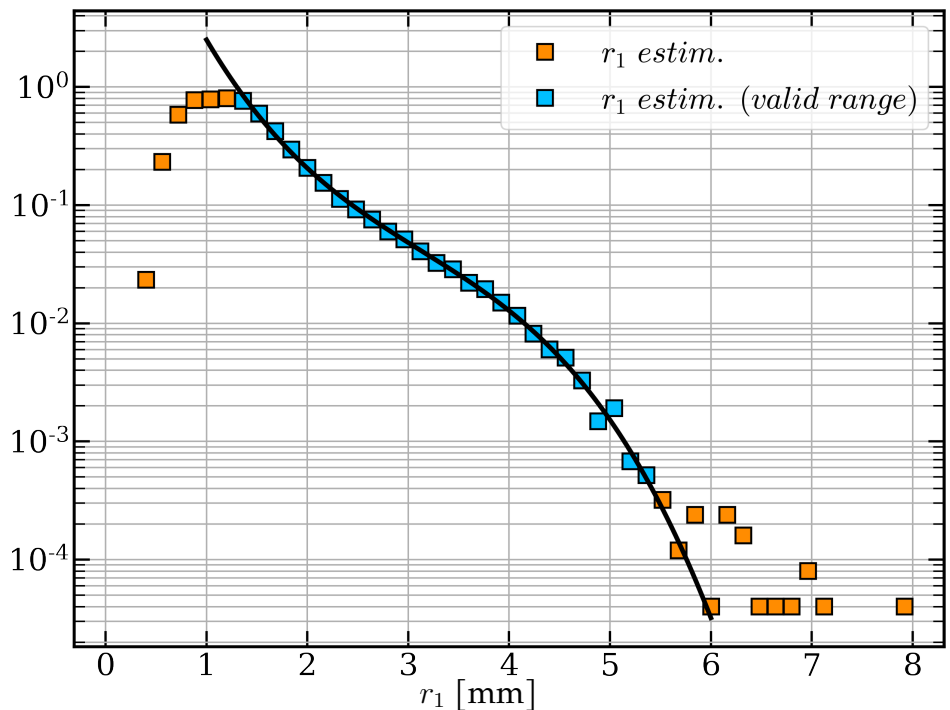


**Figure 7:** Estimation of the distribution of  $r_1$  as  $C_r \times \rho_1$ . The blue and orange points are the (normalised) histogram values. The black curve is the fourth-order polynomial fit in log-space on the blue points only (size range within which the UVP5 images copepods in a quantitative manner).

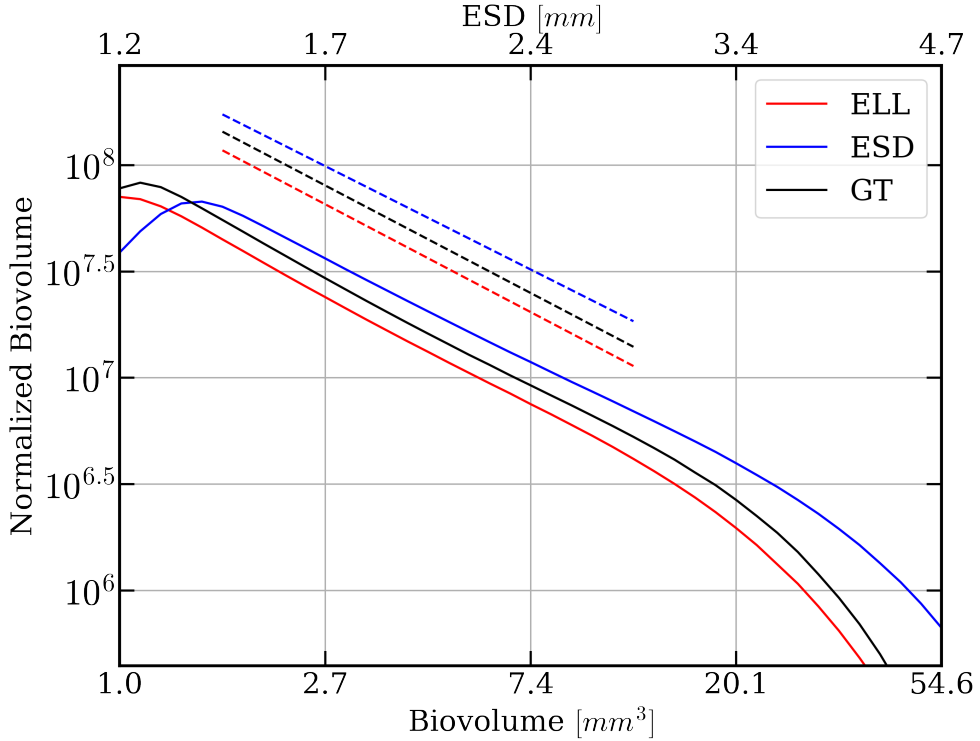


**Figure 8:** Simulated Normalized Biovolume Size Spectra (NBSS): simulated ground-truth (GT) in black; estimation from  $\mathcal{M}_{\text{ELL}}$  (resp.  $\mathcal{M}_{\text{ESD}}$ ) in red (resp. blue). The x-axis is given in volume ( $\text{mm}^3$ ) but also in Equivalent Spherical Diameter (ESD, mm) for comparability with other work. The dashed lines show the linear fits (which are offset vertically to improved readability).

### Comparison of NBSS

Following the procedure described above, a set of  $10^8$  realistic ellipsoids are generated, with  $r_1 \in [1,6]$  mm. The actual ellipsoid volumes are used to compute the simulated ground-truth NBSS. Each ellipsoid is also projected, its volume is estimated with both  $\mathcal{M}_{\text{ESD}}$  and  $\mathcal{M}_{\text{ELL}}$ , and the corresponding NBSS are computed. In all three cases, the bin size is  $0.1 \text{ mm}^3$  in log space. To assess whether the volume computation method influences the estimation of energetic transfer in the ecosystem, the slopes of a linear fit to each NBSS in the interval  $[1.7, 12.2] \text{ mm}^3$  (or  $[1.5, 2.9] \text{ mm}$ ) are computed (Fig. 8). The ground-truth NBSS is between the  $\mathcal{M}_{\text{ELL}}$  and  $\mathcal{M}_{\text{ESD}}$  ones (in the linear part at least). More importantly, the three slopes are very close to each other: -1.2 for the ground-truth vs. -1.1 for  $\mathcal{M}_{\text{ESD}}$  and -1.2

for  $\mathcal{M}_{\text{ELL}}$ . To compare this with the range of natural variability in the data set, we computed the NBSS from images collected in polar (absolute value of latitude in  $[60^\circ, 90^\circ]$ ) and temperate (absolute value of the latitude in  $[20^\circ, 40^\circ]$ ) regions, between 0 and 150m depth. The slopes of these NBSS were -0.7 (polar) and -1.4 (temperate) with  $\mathcal{M}_{\text{ESD}}$  and -0.7 and -1.6 with  $\mathcal{M}_{\text{ELL}}$ . The amplitude of natural variability is therefore much larger than the variability induced by the volume estimation method. Therefore, despite the errors the estimation methods induce on individual volume (Fig. 3), both  $\mathcal{M}_{\text{ESD}}$  and  $\mathcal{M}_{\text{ELL}}$  seem to be valid approaches to compute NBSS and to infer the energetic transfer efficiency through a linear fit.

## Discussion

We proposed a method to improve the standard estimations of the volume of copepods on images, which are based on a spherical equivalent or an ellipse fit. Our method relies on (i) more accurate measurements made on the projected silhouette and (ii) a correction factor computed from the error on the total volume due to the projection from 3D to 2D.

For the measurements, we proposed a method to estimate the projected area or to fit an ellipse on the copepod body only (Supporting Information S3), to avoid large biases caused by the antennae (and, more rarely, the uosome). Neglecting the volume of the antennae and uosome compared to that of the prosome seems appropriate in first order, and it is essentially what the standard ellipse fit does when it is not affected by antennae. Still, the validity of this assumption would need to be tested. The volumes of these different parts seem difficult to measure experimentally but could be assessed from detailed 3D scans of individuals, which we now have the technology for. A second aspect to test is whether our method indeed fits the projected silhouette better than the standard one. We noticed its does, on many images similar to Fig. 1 (see Supporting Information S3). The fact that we observed a significant reduction of the discrepancy between the total volume estimated with  $\mathcal{M}_{\text{ESD}}$  and  $\mathcal{M}_{\text{ELL}}$  when using this approach compared to the classic one also suggests a gain in accuracy. However, to assess its absolute performance, a ground-truth segmentation should be performed on a large number of images, by having human operators paint over the pixel of the image that belong to the prosome of the copepod. Then, a pixel-level match between this ground-truth and the two automated approaches (the classic one and ours) could be computed. This extremely labor-intensive effort was considered to be out of the scope of this study, especially since the proposed method is already a clear improvement over

the classic one in the worst cases (Fig. 1 and Supporting Information S3).

The core of this study is the correction of the error due to the 3D to 2D projection on the estimation of the total volume of copepods, and its application to the UVP5 data set. A potential weakness of this application is that the distributions of semi-axes ratios were estimated from a relatively small number of images (<300 for each). Since identifying copepods in a given orientation is very time consuming (and somehow subjective), a useful alternative would be to train a classifier that could automatically identify copepods seen from given angle within the total data set. Copepods were isolated from other organisms through a combination of machine learning and human classification, through the EcoTaxa application (Picheral et al., 2017). The same tools were used to train a custom classifier for side *vs.* top/bottom *vs.* other angle copepods. While it accelerated the collection of the examples in the sample sets, it did not achieve great accuracy, largely because of the overwhelming dominance of copepods seen from “other angles”.

The other assumption was in the choice of an uniform orientation distribution. While copepods in a given environment may orient themselves in a particular manner, vertically towards the surface for example (Benfield et al., 2000), quantitative information on such behaviour is very scarce. It is, however, very likely to change with location, depth, time of day, organism age, condition, etc. Since our data set contains >150k organisms of various sizes, from different locations and times, assuming a uniform distribution overall is the only possible choice. Still, to gauge the influence of the orientation distribution, we designed simulations in a non-uniform scenario and the influence on the correction factor is limited (see Supporting Information S6). In situ instruments that do not disturb the water and image in three dimensions (e.g. through holography (Katz et al., 1999)) are the only viable solution to yield quantitative information on orientation, from which an estimation of the PDF of the orientation angles could be performed. Other alternatives would be to use realistic 3D models of copepods, generate 2D views from them, and train either an image-to-orientation regressor, to directly predict the orientation, or an Augmented Auto-Encoder Convolutional Neural Network (Sundermeyer et al., 2018), to generate a view of the organism with consistent orientation from inputs taken from any angle, allowing consistent measurements on the output image.

Finally, when working on either the semi-axes ratios (for the total volume) or the semi-axes themselves (for the NBSS), we did not take into account the joint links between the three parameters  $r_1$ ,  $r_2$ , and  $r_3$ . Indeed, the data at hand only allow to study the links between  $r_1$  and  $r_2$  (side views),

and between  $r_1$  and  $r_3$  (top/bottom views). We did not have access to the triplet  $(r_1, r_2, r_3)$  for any given copepod. For this purpose, again, 3D imagery from a multi-camera system is necessary.

Overall, we showed that estimating the volume of copepods with an Equivalent Spherical Diameter assumption leads to overestimating their total volume by about 20%, while using a ellipse fit on the projection underestimates it by about 10%. Given that mesozooplankton represent a carbon biomass of 0.19 PgC in the first 200 m globally and that copepods dominate this biomass (Moriarty and O'Brien, 2013), such variations would be far from negligible for global biomass estimates from images. On a data set of 150k copepod images from the UVP5, we showed that the proposed correction method can drastically reduce the discrepancy between the two standard estimations, especially when used in conjunction with the improved area and ellipse measurements. Despite these discrepancies in the total volume, a similar simulation approach showed that the same methods yield accurate NBSS slopes, likely because the cumulated error in each size bin is similar, leading to the same slope across bins. Both methods are therefore acceptable to estimate energy transfer from size spectra measured on 2D images.

## References

- Behrenfeld, M. J., Randerson, J. T., McClain, C. R., et al. (2001). Biospheric primary production during an ENSO transition. *Science*, 291(5513):2594–2597.
- Benfield, M., Davis, C., and Gallager, S. (2000). Estimating the in-situ orientation of calanus finmarchicus on georges bank using the video plankton recorder. *Plankton Biology and Ecology*, 47:69–72.
- Bradski, G. (2000). The OpenCV library. *Dr. Dobb's Journal of Software Tools*.
- Buitenhuis, E., Le Quéré, C., Aumont, O., Beaugrand, G., Bunker, A., Hirst, A., Ikeda, T., O'Brien, T., Piontkovski, S., and Straile, D. (2006). Biogeochemical fluxes through mesozooplankton. *Global Biogeochemical Cycles*, 20(2).
- Buitenhuis, E. T., Vogt, M., Moriarty, R., Bednaršek, N., Doney, S. C., Leblanc, K., Le Quéré, C., Luo, Y.-W., O'Brien, C., O'Brien, T., Peloquin, J., Schiebel, R., and Swan, C. (2013). MAREDAT: towards a world atlas of MARine Ecosystem DATa. *Earth System Science Data*, 5(2):227–239.

- Conway, D. (2012). Identification of the copepodite developmental stages of twenty-six north atlantic copepods. occasional publication of the marine biological association no. 21 (revised edition). Technical report, Marine Biological Association of the United Kingdom, Plymouth (UK).
- de Vargas, C., Audic, S., Henry, N., et al. (2015). Ocean plankton. eukaryotic plankton diversity in the sunlit ocean. *Science*, 171314:29223618–25.
- Gorsky, G., Ohman, M. D., Picheral, M., et al. (2010). Digital zooplankton image analysis using the zooscan integrated system. *Journal of Plankton Research*, 32(3):285–303.
- Hays, G., Richardson, A., and Robinson, C. (2005). Climate change and marine plankton. *Trends in ecology & evolution*, 20:337–44.
- Hunter, J. D. (2007). Matplotlib: A 2d graphics environment. *Computing in Science & Engineering*, 9(3):90–95.
- Jones, E., Oliphant, T., Peterson, P., et al. (2001). SciPy: Open source scientific tools for Python.
- Katz, J., Donaghay, P. L., Zhang, J., King, S., and Russell, K. (1999). Submersible holocamera for detection of particle characteristics and motions in the ocean. *Deep Sea Research Part I: Oceanographic Research Papers*, 46(8):1455–1481.
- Lombard, F., Boss, E., Waite, A. M., et al. (2019). Globally consistent quantitative observations of planktonic ecosystems. *Frontiers in Marine Science*, 6:196.
- Longhurst, A. R. (2007). Chapter 9 - the atlantic ocean. In Longhurst, A. R., editor, *Ecological Geography of the Sea (Second Edition)*, pages 131–273. Academic Press, Burlington, second edition edition.
- McGill, R., Tukey, J. W., and Larsen, W. A. (1978). Variations of box plots. *The American Statistician*, 32(1):12–16.
- McKinney, W. et al. (2010). Data structures for statistical computing in python. In *Proceedings of the 9th Python in Science Conference*, volume 445, pages 51–56. Austin, TX.
- Moriarty, R. and O'Brien, T. (2013). Distribution of mesozooplankton biomass in the global ocean. *Earth System Science Data*, 5(1):45–55.

- Moriarty, R. and O'Brien, T. D. (2013). Distribution of mesozooplankton biomass in the global ocean. *Earth System Science Data*, 5(1):45–55.
- Parzen, E. (1962). On estimation of a probability density function and mode. *Ann. Math. Statist.*, 33(3):1065–1076.
- Pedregosa, F., Varoquaux, G., Gramfort, A., et al. (2011). Scikit-learn: Machine learning in python. *Journal of machine learning research*, 12(Oct):2825–2830.
- Picheral, M., Colin, S., and Irisson, J. (2017). Webplatform “EcoTaxa”, a tool for the taxonomic classification of images. <https://ecotaxa.obs-vlfr.fr/>.
- Picheral, M., Guidi, L., Stemmann, L., Karl, D. M., Iddaoud, G., and Gorsky, G. (2010). The underwater vision profiler 5: An advanced instrument for high spatial resolution studies of particle size spectra and zooplankton. *Limnology and Oceanography: Methods*, 8(9):462–473.
- Redner, R. A. and Walker, H. F. (1984). Mixture densities, maximum likelihood and the em algorithm. *SIAM Review*, 26(2):195–239.
- Scott, D. W. (1979). On optimal and data-based histograms. *Biometrika*, 66(3):605–610.
- Sprules, W. G. and Barth, L. E. (2016). Surfing the biomass size spectrum: some remarks on history, theory, and application. *Canadian Journal of Fisheries and Aquatic Sciences*, 73(4):477–495.
- Sundermeyer, M., Marton, Z.-C., Durner, M., Brucker, M., and Triebel, R. (2018). Implicit 3d orientation learning for 6d object detection from rgb images. In *The European Conference on Computer Vision (ECCV)*.
- Thiel, M., Macaya, E., Acuna, E., et al. (2007). The humboldt current system of northern and central chile. *Oceanography and marine biology*, 45:195–345.
- Van Der Walt, S., Colbert, S. C., and Varoquaux, G. (2011). The numpy array: a structure for efficient numerical computation. *ArXiv e-prints*.
- Van der Walt, S., Schönberger, J. L., Nunez-Iglesias, J., Boulogne, F., Warner, J. D., Yager, N., Gouillart, E., and Yu, T. (2014). scikit-image: image processing in python. *PeerJ*, 2:e453.

Volk, T. and Hoffert, M. I. (1985). Ocean carbon pumps: Analysis of relative strengths and efficiencies in ocean-driven atmospheric CO<sub>2</sub> changes. In Sundquist, E. T., editor, *The Carbon Cycle and Atmospheric CO<sub>2</sub> : Natural Variations Archean to Present*, volume 32 of *Geophysical monograph series*, pages 99–110. ARRAY(0xc832388), Washington, D.C.

## Acknowledgments

The authors acknowledge the projects ARTIFACTZ (joint Université Côte d’Azur and Université Laval) and WWWPIC (ANR-18-BELM-0003-01 and ANR-18-BELM-0003-02) for financial support. They also thank A McDonnell, A Rogge, A Waite, L Coppola, L Stemmann, L Karp-Boss, L Guidi, F Lombard, M Babin, R Kiko, T Biard who supervised the collection of UVP5 images through many cruises, L Drago for her help in sorting the side *vs* top/bottom copepod images, F Lombard for his advice on the NBSS work. The software development for this work was made in Python using the following open source libraries: Matplotlib (Hunter, 2007), NumPy (Van Der Walt et al., 2011), OpenCV (Bradski, 2000), Pandas (McKinney et al., 2010), Scikit-Image (Van der Walt et al., 2014), Scikit-Learn (Pedregosa et al., 2011), SciPy (Jones et al., 2001).

## Conflict of interest

None declared.

## List of Figures

- |   |   |    |
|---|---|----|
| 1 | Examples images of copepods and theirs ellipse fits: (a) top or bottom view, (b) side view. On these projections, the bodies of copepods can be well approximated by ellipses, which we assume to be ellipsoids in 3 dimensions (see Supporting Information S1). Ellipse fits on copepod images are obtained by ZooProcess (Gorsky et al., 2010) in red, affected by the antennae, and our method in green, that fits the pro-  | 4  |
| 2 | Representation of the geometrical setup of the imaging, with some notations: $r_1$ , $r_2$ , and $r_3$ the true semi-axes of an ellipsoidal object, with $r_1 \geq r_2 \geq r_3$ by convention; $\rho_1$ , $\rho_2$ the semi-axes of the projected ellipse, with $\rho_1 \geq \rho_2$ by convention; $A$ the area of the projected shape. . . . .   | 6  |
| 3 | Examples of volume estimations and errors made by $\mathcal{M}_{\text{ESD}}$ and $\mathcal{M}_{\text{ELL}}$ for an ellipsoid $E$ with $(r_1, r_2, r_3) = (12, 5, 3)$ (see Fig. 2 for the definition of $r_i$ ). The first row displays the simulated ellipse from various viewing angles. The table gives, in black, the rounded values of the volume for each method and, in colour, the percentage of under/over estimation compared to the true value, which is computed from the $r_i$ s. The individual volume estimation error is invariant to scaling (see Supporting Information S2), therefore any ellipsoid respecting $r_2/r_1 = 5/12$ and $r_3/r_1 = 3/12$ would lead to the same error percentages. The lower right plot shows the volume computed with each method for viewpoints regularly sampled along an arc turning around the ellipsoid; note that the $\mathcal{M}_{\text{ESD}}$ estimation is always greater than or equal to the $\mathcal{M}_{\text{ELL}}$ one. . . . . | 7  |
| 4 | Distributions of $r_2/r_1$ (a) and $r_3/r_1$ (b) fitted on our data set. The markers are the normalized histograms of the samples and the solid lines are the Gaussian Kernel Density Estimates.  | 15 |

5	Total volume estimated by $\mathcal{M}_{\text{ESD}}$ (blue) or $\mathcal{M}_{\text{ELL}}$ (red) obtained by ZooProcess ( $ZP$ ) and our improved measures, uncorrected ( $W^u$ ) or corrected ( $W^c$ ). The discrepancies between the methods are highlighted by dashed lines and annotated by the corresponding absolute differences. The proposed correction drastically reduces these discrepancies, although there is no way to tell which result would be more realistic between $\mathcal{M}_{\text{ESD}}$ or $\mathcal{M}_{\text{ELL}}$ before correction. . . . .	16
6	(a) Relationship between $r_2$ and $r_1$ from 254 copepods seen from the side, for $r_1 > 1$ mm. (b) Relationship between $r_3$ and $r_1$ from the 173 copepods seen from the top or bottom, for $r_1 > 1$ mm. The colored dashed line are linear regressions fits, significant in both cases ( $p < 0.01$ , $R^2 = 88\%$ for (a) and $R^2 = 75\%$ for (b)). The color scale of points represents the density of samples. . . . .	18
7	Estimation of the distribution of $r_1$ as $C_r \times \rho_1$ . The blue and orange points are the (normalised) histogram values. The black curve is the fourth-order polynomial fit in log-space on the blue points only (size range within which the UVP5 images copepods in a quantitative manner). . . . .	19
8	Simulated Normalized Biovolume Size Spectra (NBSS): simulated ground-truth (GT) in black; estimation from $\mathcal{M}_{\text{ELL}}$ (resp. $\mathcal{M}_{\text{ESD}}$ ) in red (resp. blue). The x-axis is given in volume ( $\text{mm}^3$ ) but also in Equivalent Spherical Diameter (ESD, mm) for comparability with other work. The dashed lines show the linear fits (which are offset vertically to improved readability). . . . .	20
S1.1	Geometrical setup of the ellipsoid model. The camera is represented by its optical center $e$ , the sensor plane $\Pi$ , and the sensor orthonormal coordinate system $(O_\Pi, u, v)$ . The global orthonormal coordinates system is represented by $(O, i, j, k)$ . The axes $i$ and $u$ are parallel, and so are $j$ and $v$ . The ellipsoid center is at distance $\delta$ from $\Pi$ and $\epsilon$ from $e$ . Without loss of generality (for our problem), the ellipsoid center is at $O$ , and $e$ is on the axis $k$ with the optical axis aligned with $k$ . Consequently, $O_\Pi$ is also on the axis $k$ . . . . .	S1.2

S3.1	Copepod body mask computation as a common preliminary step for surface estimation and ellipse fit. Reading the figure in lexicographical order, each image is the result of the processing of the previous one. They are: (a) the input grayscale image, (b) the binary mask obtained by thresholding, (c) the inner distance map, (d) the eroded mask obtained by thresholding, (e) the outer distance map, and (f) the dilated mask obtained by thresholding (same threshold). . . . .	S3.2
S3.2	Multiple examples of ellipse fit based on the original mask in green and for the new proposed method in red. We see that when antennae are not visible, the result is almost the same, but when they are visible, the classic method is not appropriate. . . . .	S4.1
S5.1	Kernel density estimate of the latitudinal distribution of the images of all copepods and of the side or top/bottom views.	S5.1
S5.2	Distribution of the length of the semi-major axis of the ellipse fitted in the two views of the copepods. The vertical axis is the number of observations, in $\log_{10}$ scale. The horizontal axis is the semi-major axis $r_1$ , which is equal to $\rho_1$ in these viewpoints and approximates the half of the prosome length, in millimeters. . . . .	S5.2
S6.1	(a) Distribution of $r_3/r_1$ for various mixtures of two subpopulations, from $\alpha = 0$ (Normal distribution fitted on the $r_2/r_1$ data of the UVP5 experiment), to $\alpha = 1$ , Beta distribution with parameters $a = 2$ and $b = 15$ . (b) The corresponding correction factors for $N = 10^6$ ellipsoids. The black dashed line indicates a correction factor of one, i.e. no error. . . . .	S6.2
S6.2	Evolution of the correction factors for varying ranges of allowed vertical rotation. The rotation angle around the y-axis, $\theta$ , is restricted to the interval $[0, \theta_{\max}]$ . Each dot of the plots corresponds to a simulation for a particular $\theta_{\max}$ . The black dashed line indicates a correction factor of one, i.e. no error. . . . .	S6.3
S7.1	Corrections factors ((a) $\mathcal{M}_{\text{ESD}}$ , (b) $\mathcal{M}_{\text{ELL}}$ ) for $N_i = 10^i, i \in \{3, 4, 5, 6, 7\}$ . For each $i$ , we computed the correction factors 50 times. The blue (red) line is the mean factor for the $\mathcal{M}_{\text{ESD}}$ ( $\mathcal{M}_{\text{ELL}}$ ) method. The boxes and whiskers are drawn according to Tukey's definition (McGill et al., 1978). . . . .	S7.2

# S1 Projection of an ellipsoid

## S1.1 Geometrical setup

A centered ellipsoid is defined by all 3-dimensional vectors verifying

$$x^\top M x = 1 \quad (14)$$

where  $M$  is a positive definite<sup>1</sup>  $3 \times 3$ -matrix whose elements are denoted by  $m_{ij}$ . Let  $(i, j, k)$  denote an orthonormal basis, and let  $O$  denote the origin. To study how this ellipsoid projects onto a plane using perspective projection, let us define (i) an optical center  $e$

$$e = \begin{bmatrix} 0 \\ 0 \\ -\epsilon \end{bmatrix} \quad (15)$$

where  $\epsilon > 0$  is such that  $e$  is outside the ellipsoid, and (ii) a projection plane  $\Pi$  described by its normal

$$n = \begin{bmatrix} 0 \\ 0 \\ 1 \end{bmatrix} \quad (16)$$

and its distance  $\delta$ ,  $\epsilon > \delta > 0$ , to the origin such that  $\Pi$  does not intersect the ellipsoid. The plane  $\Pi$  is equipped with the orthonormal basis  $(u, v)$  where  $u$  and  $v$  correspond to  $i$  and  $j$  respectively. Its origin  $O_\Pi$  is located at the intersection between  $\Pi$  and the segment linking  $e$  to  $O$ . All these elements are illustrated on Fig. S1.1.

## S1.2 Ellipsoid silhouette in 3-D

For some unit vector  $d$ , let  $x$  be defined as

$$x = e + \tau d \quad (17)$$

with  $\tau > 0$  and  $d \cdot n > 0$ . The ellipsoid silhouette as seen from  $e$  is given by the set of vectors  $d$  such that the half-line described by  $x$  when  $\tau$  varies is tangent to the ellipsoid<sup>2</sup>.

The point  $x$  is on the ellipsoid if and only if

$$(d^\top M d)\tau^2 + (2d^\top M e)\tau + (e^\top M e - 1) = 0, \quad (18)$$

---

<sup>1</sup>positive definite matrices are, by definition, symmetric

<sup>2</sup>for such a vector  $d$ , there is a corresponding value for  $\tau$

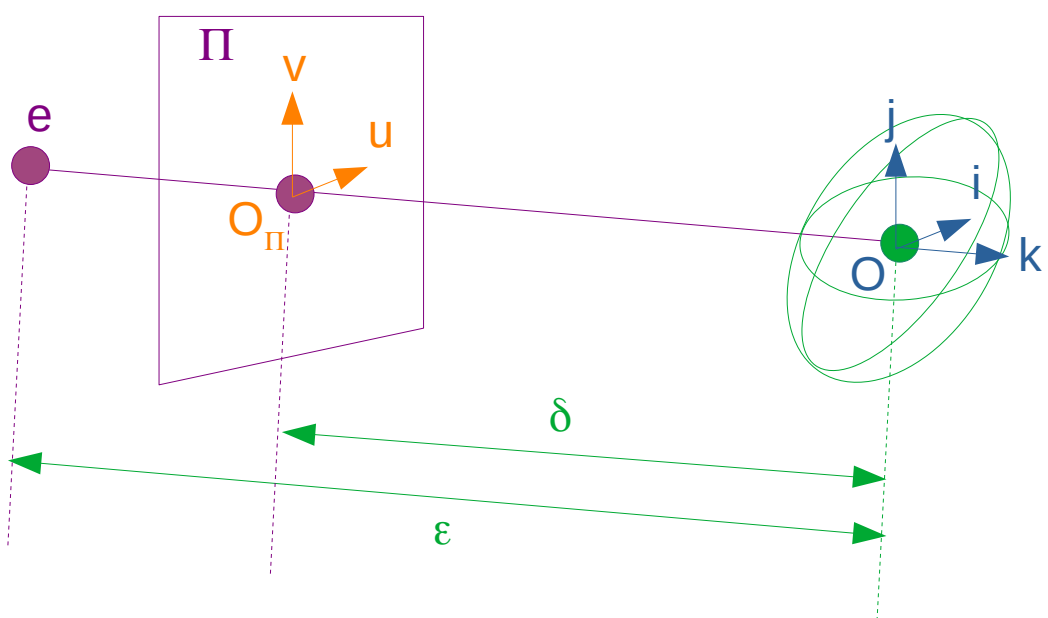


**Figure S1.1:** Geometrical setup of the ellipsoid model. The camera is represented by its optical center  $e$ , the sensor plane  $\Pi$ , and the sensor orthonormal coordinate system  $(O_\Pi, u, v)$ . The global orthonormal coordinates system is represented by  $(O, i, j, k)$ . The axes  $i$  and  $u$  are parallel, and so are  $j$  and  $v$ . The ellipsoid center is at distance  $\delta$  from  $\Pi$  and  $\epsilon$  from  $e$ . Without loss of generality (for our problem), the ellipsoid center is at  $O$ , and  $e$  is on the axis  $k$  with the optical axis aligned with  $k$ . Consequently,  $O_\Pi$  is also on the axis  $k$ .

which is of the form

$$\alpha\tau^2 + \beta\tau + \gamma = 0. \quad (19)$$

Therefore, the half-line described by  $x$  is tangent to the ellipsoid if and only if Eq. (19) has a unique solution<sup>3</sup>, that is if and only if  $\beta^2 - 4\alpha\gamma = 0$ , which is equivalent to

$$d^\top S d = 0 \quad (20)$$

where  $S$  is equal to

$$S = M e e^\top M + (1 - e^\top M e) M. \quad (21)$$

The ellipsoid silhouette is defined by the solutions of Eq. (20) respecting, as mentioned earlier, the following two conditions:  $|d| = 1$  and  $d \cdot n > 0$ .

Let  $S_\epsilon$  be defined as

$$S_\epsilon = \frac{1}{\epsilon^2} S. \quad (22)$$

Note that  $S_\epsilon$  can be used in Eq. (20) in place of  $S$ . To propose a more explicit form of  $S_\epsilon$ , let us use the following block matrix formulation

$$M = \left[ \begin{array}{c|c} M_{11} & M_{21}^\top \\ \hline M_{21} & m_{33} \end{array} \right] \quad (23)$$

where  $M_{11}$  is a  $2 \times 2$ -matrix,  $M_{21}$  is a  $1 \times 2$ -vector, and  $m_{33}$  is a scalar. Using such a block formulation, we have

$$e e^\top = \left[ \begin{array}{c|c} 0_{11} & 0_{21}^\top \\ \hline 0_{21} & \epsilon^2 \end{array} \right] \quad (24)$$

where  $0_{ij}$  denotes a matrix of zeros matching the dimension of  $M_{ij}$ .

Then

$$M e e^\top M = \epsilon^2 \left[ \begin{array}{c|c} M_{21}^\top M_{21} & m_{33} M_{21}^\top \\ \hline m_{33} M_{21} & m_{33}^2 \end{array} \right]. \quad (25)$$

Similarly

$$e^\top M e = \epsilon^2 m_{33}. \quad (26)$$

Therefore

$$S_\epsilon = \left[ \begin{array}{c|c} M_{21}^\top M_{21} & m_{33} M_{21}^\top \\ \hline m_{33} M_{21} & m_{33}^2 \end{array} \right] - \left( m_{33} - \frac{1}{\epsilon^2} \right) M \quad (27)$$

$$= \left[ \begin{array}{c|c} M_{21}^\top M_{21} - m'_{33} M_{11} & (m_{33} - m'_{33}) M_{21}^\top \\ \hline (m_{33} - m'_{33}) M_{21} & (m_{33} - m'_{33}) m_{33} \end{array} \right] \quad (28)$$

---

<sup>3</sup>for completeness, note that this unique solution is  $\tau = -\frac{\beta}{2\alpha}$ .

where  $m'_{33}$  is defined as

$$m'_{33} = m_{33} - \frac{1}{\epsilon^2}. \quad (29)$$

So finally

$$S_\epsilon = \left[ \begin{array}{c|c} M_{21}^\top M_{21} - m'_{33} M_{11} & (1/\epsilon^2) M_{21}^\top \\ \hline (1/\epsilon^2) M_{21} & (1/\epsilon^2) m_{33} \end{array} \right]. \quad (30)$$

### S1.3 2-D silhouette

As mentioned earlier, Eq. (20) defines the silhouette of the ellipsoid in a perspective projection setup. On plane  $\Pi$ , this silhouette is defined by points  $p$  such that, for all solutions  $d$  to Eq. (20),

$$\begin{cases} p = e + \tau' d \\ (p - e) \cdot n = \epsilon - \delta \end{cases} \quad (31)$$

where  $\tau'$  is a scalar<sup>4</sup>. The first equation of (31) is equivalent to

$$d = \frac{1}{\tau'}(p - e). \quad (32)$$

Equation (20) can now be rewritten in terms of  $p$  (and  $S_\epsilon$  as noted earlier) as follows

$$(p - e)^\top S_\epsilon(p - e) = 0. \quad (33)$$

The point  $p$  can be written as

$$p = O_\Pi + q \quad (34)$$

where  $q$  is a vector whose third component is equal to 0. Using a block formulation, we have

$$q = \begin{bmatrix} q_1 \\ 0 \end{bmatrix} \quad (35)$$

and

$$S_\epsilon = \left[ \begin{array}{c|c} S_{11} & S_{21}^\top \\ \hline S_{21} & s_{33} \end{array} \right]. \quad (36)$$

Then, Eq. (33) is equivalent to

$$q_1^\top P q_1 + Q q_1 = r \quad (37)$$

---

<sup>4</sup>combining the two equations of (31) together, one gets  $\tau' = (\epsilon - \delta)/(d \cdot n)$

where<sup>5</sup>

$$P = S_{11}, \quad (38)$$

$$Q = 2(\epsilon - \delta)S_{21}, \quad (39)$$

$$r = -(\epsilon - \delta)^2 s_{33}. \quad (40)$$

One recognizes the equation of an ellipse which can be put into the following standard form

$$(q_1 - c)^\top \left( \frac{1}{r - Qc/2} P \right) (q_1 - c) = 1 \quad (41)$$

where  $c = -P^{-1}Q^\top/2$  is the center of the ellipse.

## S1.4 Semi-axes for perspective projection

Let  $\lambda_1$  and  $\lambda_2$  be the two (positive) eigenvalues of  $P$ ,  $\lambda_1 \leq \lambda_2$ . Then the semi-minor and semi-major axes of the ellipse defined by Eq. (41) are

$$\rho_i = \sqrt{\frac{r - Qc/2}{\lambda_i}}, i \in \{1, 2\}. \quad (42)$$

Gathering everything together,  $\rho_i$  can be rewritten in terms of  $M$  as follows

$$r = -(1 - \delta/\epsilon)^2 m_{33}, \quad (43)$$

$$Q = 2\frac{\epsilon - \delta}{\epsilon^2} M_{21}, \quad (44)$$

$$P = M_{21}^\top M_{21} - \left( m_{33} - \frac{1}{\epsilon^2} \right) M_{11}, \quad (45)$$

$$c = -P^{-1}Q^\top/2, \quad (46)$$

$$\lambda_i = (\text{tr}(P) + \sigma_i \sqrt{\Delta})/2, \quad (47)$$

$$|\sigma_i| = 1 \text{ and } \sigma_1 \sigma_2 = -1, \quad (48)$$

$$\Delta = \text{tr}(P)^2 - 4 \det(P) \quad (49)$$

where  $\text{tr}(P)$  is the trace of  $P$ ,  $\det(P)$  is its determinant, and the  $\sigma_i$ 's are chosen so that  $\rho_1 \geq \rho_2$ .

---

<sup>5</sup>in case  $P$  is definite negative,  $P$ ,  $Q$  and  $r$  must be replaced with their opposite

## S1.5 Semi-axes for parallel projection

From the previous section, it follows that, for a parallel projection (i.e.  $\epsilon = \infty$ ), the semi-minor and semi-major axes have the following simpler expression

$$\rho_i = \sqrt{\frac{m_{33}}{\lambda_i}}, i \in \{1, 2\} \quad (50)$$

and

$$P = m_{33}M_{11} - M_{21}^T M_{21}, \quad (51)$$

while  $\lambda_i$ ,  $\sigma_i$ , and  $\Delta$  are unchanged. Note that  $\delta$  no longer appears in the equations.

## S2 Invariance of volume estimation error to scaling

### S2.1 Individual volume

This section has no direct practical application. It only presents developments useful in Supporting Information S2.2.

For an axis-aligned ellipsoid,  $M$  is diagonal. The diagonal components are related to the semi-axes  $r_i$  as follows

$$m_{ii} = r_i^{-2}, i \in \{1, 2, 3\}. \quad (52)$$

The ellipsoid volume is then classically given by

$$V = \frac{4}{3}\pi r_1 r_2 r_3 \quad (53)$$

$$= \frac{4}{3} \frac{\pi}{\sqrt{m_{11} m_{22} m_{33}}}. \quad (54)$$

For a general ellipsoid (i.e., any orientation), the volume is

$$V = \frac{4}{3} \frac{\pi}{\sqrt{\det(M)}} \quad (55)$$

where  $\det(M)$  is the determinant of  $M$ . Let  $V_*$  denote an estimation of the true volume  $V$ , where \* is ESD or ELL here. The relative error in volume estimation is defined as

$$\mathcal{E}_* = \frac{V_*}{V}. \quad (56)$$

For writing Eq. (56) for the  $\mathcal{M}_{\text{ESD}}$ , it should be reminded that, since the projection silhouette is an ellipse of area  $\pi\rho_1\rho_2$ , the equivalent radius is equal to  $\sqrt{\rho_1\rho_2}$ . Then, the relative errors of the  $\mathcal{M}_{\text{ESD}}$  or  $\mathcal{M}_{\text{ELL}}$  methods are

$$\mathcal{E}_{\text{ESD}} = (\rho_1\rho_2)^{3/2} \sqrt{\det(M)} \quad \text{See Eq. (1)} \quad (57)$$

$$\mathcal{E}_{\text{ELL}} = \rho_1\rho_2^2 \sqrt{\det(M)}. \quad \text{See Eq. (2)} \quad (58)$$

The following section demonstrates the invariance of these individual volume estimation errors to scaling, a mathematical result that strongly impact the practical procedure (see Section “Simulation of copepod bodies”).

### S2.2 Invariance of individual volume estimation error to scaling

This section has no direct practical application. It only presents developments useful in Supporting Information S2.3.

### S2.2.1 Common remarks

The purpose is to show that  $\mathcal{E}_{\text{ESD}}$  and  $\mathcal{E}_{\text{ELL}}$  do not depend on the absolute volume of the ellipsoid, which is a function of  $(r_1, r_2, r_3)$ , but rather on the ellipsoid proportions  $(r_2/r_1, r_3/r_1)$ . One way to prove this statement is to show that  $\mathcal{E}_*(\alpha M) = \mathcal{E}_*(M)$  for any  $\alpha > 0$ . Indeed, if this holds, then choosing  $\alpha$  equal to  $r_1^2$  implies that  $\alpha M$  is defined by the triplet  $(1, r_2/r_1, r_3/r_1)$ .

Let  $\rho$ , resp.  $\lambda$ , be a generic notation for  $\rho_1$  and  $\rho_2$ , resp.  $\lambda_1$  and  $\lambda_2$ . The other useful reminders are

$$\rho = \sqrt{\frac{m_{33}}{\lambda}} \quad (59)$$

$$\lambda : \text{eigenvalue of } P \quad (60)$$

$$P = m_{33}M_{11} - M_{21}^T M_{21}. \quad (61)$$

Let us add a subscript  $\alpha$  to these quantities to denote their expressions when  $M$  is replaced with  $\alpha M$ . We have

$$m_{33,\alpha} = \alpha m_{33} \quad (62)$$

$$P_\alpha = \alpha^2 P. \quad (63)$$

It is also clear that if  $\lambda$  is an eigenvalue of  $P$ , then  $\beta\lambda$  is an eigenvalue of  $\beta P$  ( $Px = \lambda x \Rightarrow \beta Px = \beta\lambda x$ ) for any  $\beta \neq 0$ . Therefore,

$$\lambda_\alpha = \alpha^2 \lambda. \quad (64)$$

Hence, it can be concluded that

$$\rho_\alpha = \frac{\rho}{\sqrt{\alpha}}. \quad (65)$$

Finally, note that we have the following property on the matrix determinant

$$\det(\alpha M) = \alpha^3 \det(M) \quad (66)$$

if  $M$  is a  $3 \times 3$ -matrix.

### S2.2.2 $\mathcal{M}_{\text{ESD}}$ method

As a reminder, the relative error in volume estimation of the  $\mathcal{M}_{\text{ESD}}$  method is

$$\mathcal{E}_{\text{ESD}}(M) = \mathcal{E}_{\text{ESD}}(r_1, r_2, r_3, \xi) \quad (67)$$

$$= (\rho_1 \rho_2)^{3/2} \sqrt{\det(M)}. \quad (68)$$

Then

$$\mathcal{E}_{\text{ESD}}(\alpha M) = (\rho_{1,\alpha} \rho_{2,\alpha})^{3/2} \sqrt{\det(\alpha M)} \quad (69)$$

$$= \frac{(\rho_1 \rho_2)^{3/2}}{\sqrt{\alpha^3}} \sqrt{\alpha^3 \det(M)} \quad (70)$$

$$= \mathcal{E}_{\text{ESD}}(M). \quad (71)$$

### S2.2.3 $\mathcal{M}_{\text{ELL}}$ method

As a reminder, the relative error in volume estimation of the  $\mathcal{M}_{\text{ELL}}$  method is

$$\mathcal{E}_{\text{ELL}}(M) = \mathcal{E}_{\text{ELL}}(r_1, r_2, r_3, \xi) \quad (72)$$

$$= \rho_1 \rho_2^2 \sqrt{\det(M)}. \quad (73)$$

Then

$$\mathcal{E}_{\text{ELL}}(\alpha M) = \rho_{1,\alpha} \rho_{2,\alpha}^2 \sqrt{\det(\alpha M)} \quad (74)$$

$$= \frac{\rho_1 \rho_2^2}{\alpha \sqrt{\alpha}} \sqrt{\alpha^3 \det(M)} \quad (75)$$

$$= \mathcal{E}_{\text{ELL}}(M). \quad (76)$$

## S2.3 Invariance of total volume estimation error to scaling

Let  $V^i, i \in [1..n]$ , be a set of (true) ellipsoid volumes, and let  $V_*^i$  and  $\mathcal{E}_*^i$  be some corresponding estimated volumes by the method “\*” and the associated individual volume estimation errors, respectively. The total volume estimation error is

$$\mathcal{T}_* = \frac{\sum_i V_*^i}{\sum_i V^i} = \frac{\bar{V}_*}{\bar{V}} \quad (77)$$

where  $\bar{X}$  denotes the average of  $X$ . Now, suppose that each ellipsoid volume is scaled by a factor  $\alpha_i$  ( $U^i = \alpha_i V^i$ ), for example as a result of the normalization of the ellipsoids by dividing their semi-axes  $r_1^i, r_2^i$ , and  $r_3^i$  by  $r_1^i$ . How will the estimated volumes  $U_*^i$  vary with respect to  $V_*^i$ ? From Supporting Information S2.2, we know that  $\mathcal{E}_*^i = V_*^i / V^i$  is invariant to ellipsoid scaling when “\*” is ESD or ELL. Therefore,  $U_*^i / U^i$  must still be equal to  $\mathcal{E}_*^i$ , which implies that  $U_*^i = \alpha_i V_*^i$ . Hence, the total volume estimation error after scaling is

$$\mathcal{T}'_* = \frac{\sum_i U_*^i}{\sum_i U^i} = \frac{\sum_i \alpha_i V_*^i}{\sum_i \alpha_i V^i} = \frac{\overline{\alpha} \bar{V}_*}{\overline{\alpha} \bar{V}}. \quad (78)$$

The covariance between two random variables, say a factor  $\alpha$  and a volume  $V$ , can be written in terms of expected values as follows

$$\text{Cov}(\alpha, V) = E[\alpha V] - E[\alpha] E[V]. \quad (79)$$

The situation of practical interest here is when  $\alpha$  is related to the normalization of the ellipsoids, in which case  $V$  and  $\alpha$  are not independent (which would otherwise immediately guarantee that  $\text{Cov}(\alpha, V) = 0$ ). Indeed,

$$\alpha = \frac{1}{r_1^3} \quad (80)$$

$$V = \frac{4}{3}\pi r_1 r_2 r_3. \quad (81)$$

However, they are not correlated (i.e., their relationship is not linear). Consequently, their covariance is equal to zero and

$$E[\alpha V] = E[\alpha] E[V]. \quad (82)$$

The same conclusion can be drawn regarding the estimated volume  $V_*$ . If the number of samples  $n$  is large enough, these results can be safely extended to average values so that

$$\overline{\alpha V} \simeq \bar{\alpha} \bar{V} \quad (83)$$

$$\overline{\alpha V_*} \simeq \bar{\alpha} \bar{V}_*. \quad (84)$$

In the end,

$$\mathcal{T}'_* \simeq \frac{\bar{\alpha} \bar{V}_*}{\bar{\alpha} \bar{V}} = \mathcal{T}_*. \quad (85)$$

This concludes the proof that, if the number of involved volumes is high enough, the total volume estimation error is largely invariant to scaling. As a consequence, the randomly generated ellipsoids used to determine the total volume correction factor (see Sections “Simulation of copepod bodies” and “Corrected total volume”, and, in particular, Eq. (12)) can be safely normalized, for example by dividing their semi-axes by their largest one.

## S3 Improved surface estimation and ellipse fitting

### S3.1 Common steps

The general idea of the improved methods proposed in this appendix is to get rid of the antennae (and tail) before measuring the copepod silhouette surface or fitting an ellipse onto it. It is assumed that the binary mask of the copepod has been determined previously. We propose to compute the Inner Distance Map (IDM) of this mask and to erode it using a threshold. We fix the threshold to  $\text{max(IDM)}/2.1$  in our experiments. This step allows to get rid of the antennae. Note that the binary mask could have been eroded directly using mathematical morphology. However, it would make use of a discrete so-called structural element (typically a discretized disk), which would lead to a coarser eroded shape. Given the small size of a copepod in our images, this could have a negative impact on the subsequent steps. Next, to recover the original copepod body size, the outer distance map of the eroded mask is computed and thresholded using the same threshold as the one used for erosion. This amounts to dilate the eroded mask, but again in a finer way than if using mathematical morphology. The various steps are illustrated in Fig. S3.1. A Python implementation is available at: <https://gitlab.inria.fr/cedubois/Copepod-Volume-Correction>.

### S3.2 Surface estimation

The copepod surface estimation is performed by counting the number of pixels of its binary mask. The improved version simply counts the pixels of the mask obtained in Supporting Information S3.1 as opposed to counting the pixels in the original binary mask which includes the antennae.

### S3.3 Ellipse fitting

When an object is described by a binary mask of pixels, the most classical ellipse fitting method interprets the pixels as the samples of a point cloud. The covariance matrix of the cloud is computed. Its eigenvectors represent the best fitting ellipse orientation while its eigenvalues represent the semi-axes of the ellipse. A simple improvement of this method (or any other ellipse fitting method as a matter of fact) consists in rescaling the ellipse so that its area matches the object area. This is implemented by the software ImageJ that ZooProcess (ZP), the software used to process UVP images,

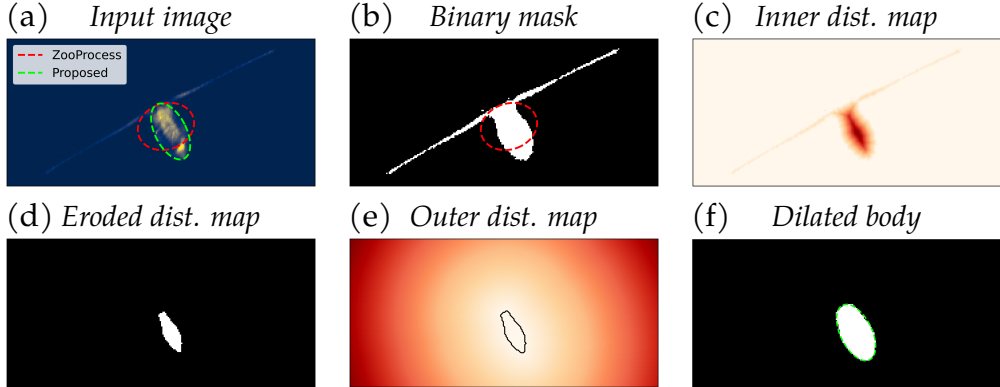


**Figure S3.1:** Copepod body mask computation as a common preliminary step for surface estimation and ellipse fit. Reading the figure in lexicographical order, each image is the result of the processing of the previous one. They are: (a) the input grayscale image, (b) the binary mask obtained by thresholding, (c) the inner distance map, (d) the eroded mask obtained by thresholding, (e) the outer distance map, and (f) the dilated mask obtained by thresholding (same threshold).

uses. However, if this improvement allows to correct the fitted ellipse surface (which can be enough for some applications), it does not help that much for copepod volume estimation. Indeed, the precision of the small semi-axis is crucial, and it is not improved by the surface adjustment. As a reminder, the  $\mathcal{M}_{\text{ELL}}$  estimation of the volume is:

$$V_{\text{ELL}} = \frac{4}{3}\pi\rho_1\rho_2^2 = \underbrace{\frac{4}{3}\pi\rho_1\rho_2}_{\text{Surface}} \underbrace{\rho_2}_{\text{Minor semi-axis}}. \quad (86)$$

Alternatively, the ellipse could be fitted on the grayscale version of the object, that is using the pixel intensities as sample weights when computing the covariance matrix. However, we found that this alternative does not work well on the copepod images of our data set.

Whatever the ellipse fitting method is, the starting point is the copepod mask. The fitting methods get distracted by the antennae, which can result in very bad ellipses (see the red ellipses in Fig. S3.2). Therefore, we proposed to fit an ellipse on the mask obtained in Supporting Information S3.1 instead of the original binary mask which includes the antennae (see the green ellipses in Fig. S3.2).

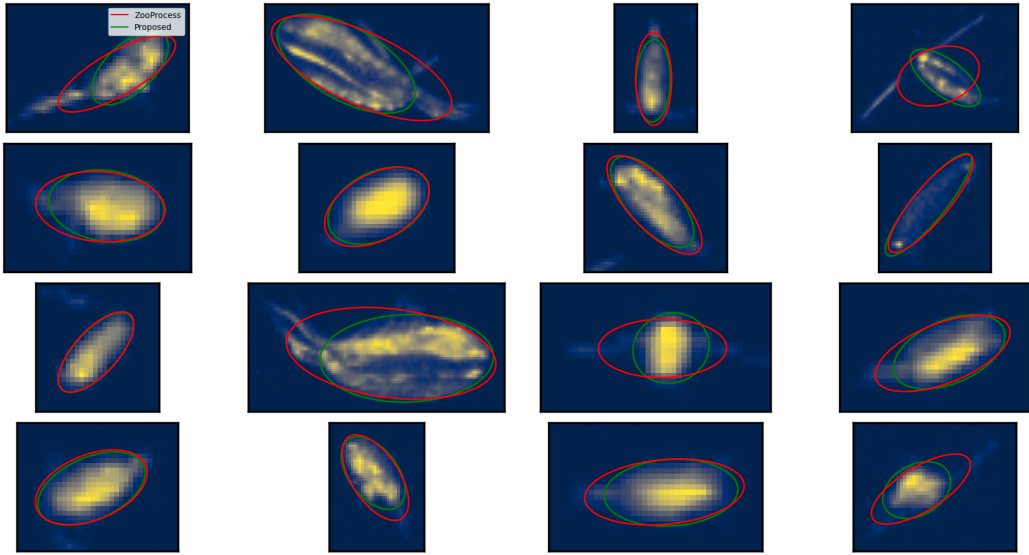


**Figure S3.2:** Multiple examples of ellipse fit based on the original mask in green and for the new proposed method in red. We see that when antennae are not visible, the result is almost the same, but when they are visible, the classic method is not appropriate.

## S4 The proposed method, step-by-step

This section gathers the results of the different sections into a step-by-step procedure for estimating the total volume of copepods given a data set of 2-D views. It is composed of two stages: a learning stage which has to be performed once for all, or whenever the expert thinks the proposed simulation procedure must be adapted to the data, and a “usage” stage which can be applied at will.

### S4.1 Learning stage

1. Generate random ellipsoid samples that realistically represent a generic population of copepods, or a population following some characteristics inferred from the data set. The randomness must be constrained by the expert knowledge in the form of specific simulation parameters.
2. Compute the total volume of the ellipsoid samples. This represents the true total volume. See Eqs. (4) and (12).
3. For each ellipsoid sample, compute the projection ellipse (see Eq. (7)) and the estimated volume using either the  $\mathcal{M}_{\text{ESD}}$  (see Eq. (1)) or the

$\mathcal{M}_{\text{ELL}}$  method (see Eq. (2)).

4. Sum all the estimated volumes to get the estimated total volume.
5. Compute the total volume estimation error  $\mathcal{T}_*$  from the true and estimated total volumes (see Eq. (12)). This is the final product of the learning stage.

## S4.2 “Usage” stage

1. For each copepod image of a data set, determine the copepod silhouette using an image segmentation method. On UVP images, a simple binarization using a fixed threshold is enough.
  - 1.a. For the  $\mathcal{M}_{\text{ESD}}$  method, compute the silhouette area  $A$  (see Supporting Information S3.2) and the corresponding estimated volume (see Eq. (1)).
  - 1.b. For the  $\mathcal{M}_{\text{ELL}}$  method, fit an ellipse onto the silhouette (see Supporting Information S3.3). Let  $\rho_1$  and  $\rho_2$  be the semi-major and semi-minor axes, respectively. Then compute the corresponding estimated volume (see Eq. (2)).
2. Sum all the estimated volumes to get the estimated total volume  $\tilde{W}_*$  where \* is either ESD or ELL.
3. Compute the corrected total volume estimation  $\hat{W}_*$  by dividing  $\tilde{W}_*$  with  $\mathcal{T}_*$  from the learning stage (see Eq. (13)).

## S4.3 Algorithmic details

### S4.3.1 Uniformly random rotations

This section defines the rotation matrices used to simulate random orientations of ellipsoids.

In order to generate an ellipsoid with a uniformly random orientation, we generate a random rotation matrix  $R$  and rotate an axis-aligned ellipsoid with it. The generation of an axis-aligned ellipsoid is described in Section “Simulation of copepod bodies”. If the axis-aligned ellipsoid is represented by a matrix  $M$  (see Section “Principle for correction of total volume”), then the rotated ellipsoid is represented by the matrix

$$M_{\text{rot}} = RMR^T. \quad (87)$$

A general rotation matrix can be defined using three elementary rotation

matrices

$$R = R_z(\Phi)R_y(\Theta)R_x(\Psi) \quad (88)$$

with  $R_i(\alpha)$ ,  $i \in \{x, y, z\}$ , defines the rotation by angle  $\alpha$  around axis  $i$ . To generate a random rotation matrix, one has to randomly choose the angle triplet  $(\Psi, \Theta, \Phi)$ . In order to guarantee the uniformity of the ellipsoid orientations, the angles  $\Psi$ ,  $\Theta$ , and  $\Phi$  must be distributed adequately, that is

$$\Psi = U[0, 2\pi[ \quad (89)$$

$$\Theta = \arccos(1 - 2U[0, 1[) - \frac{\pi}{2} \quad (90)$$

$$\Phi = U[0, 2\pi[ \quad (91)$$

where  $U[a, b[$  is the uniform distribution between  $a$  (included) and  $b$  (excluded).

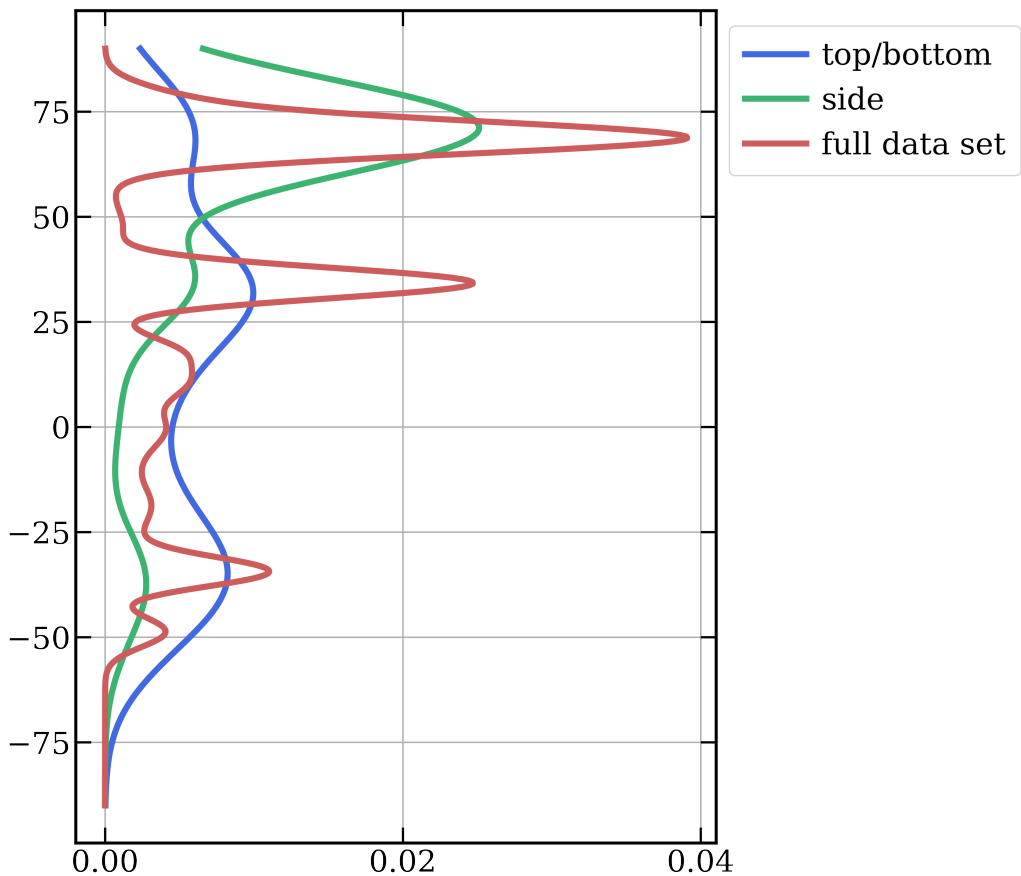


**Figure S5.1:** Kernel density estimate of the latitudinal distribution of the images of all copepods and of the side or top/bottom views.

## S5 Distribution of selected sample images

To define the real-world distribution of the semi axes of the ellipsoid representing the body of copepods ( $r_1$ ,  $r_2$ , and  $r_3$ ) as well as the ratios between them, defining the shape of the ellipsoid ( $r_2/r_1$  and  $r_3/r_1$ ), 295 copepods seen from the side (on which  $r_1$  and  $r_2$  are measurable) and 265 copepods seen from the top or bottom (on which  $r_1$  and  $r_3$  are measurable) were manually curated from a collection of >150k images. To make sure that these small samples were representative of the whole data set, we checked their latitudinal and size (i.e.  $r_1$ ) distributions. The shape of the latitudinal distribution of the side and top/bottom views matches well that of the total data set (Fig. S5.1). The side views shows an excess at high latitude, likely linked with a bias in the size distribution (see below; copepods are larger at

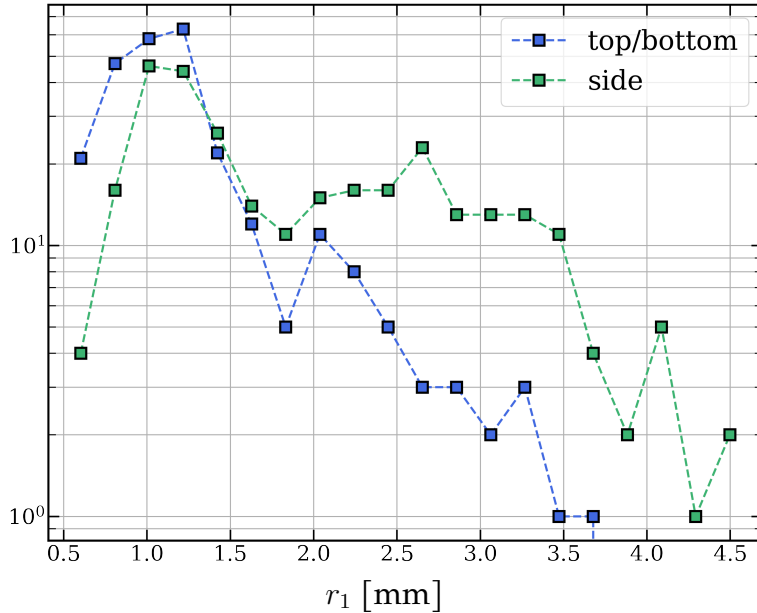


**Figure S5.2:** Distribution of the length of the semi-major axis of the ellipse fitted in the two views of the copepods. The vertical axis is the number of observations, in  $\log_{10}$  scale. The horizontal axis is the semi-major axis  $r_1$ , which is equal to  $\rho_1$  in these viewpoints and approximates the half of the prosome length, in millimeters.

high latitudes), and a linked under-representation elsewhere. The pattern is opposite for the top-bottom views. However, no region is completely missed in the samples and even some details of the distribution (such as the two peaks around  $-40^\circ$ ) are captured. Therefore, we consider them representative enough. The theoretical expectation for the length distribution is an exponential decay (Sprules and Barth, 2016), i.e. a linear decrease, in log-scale. This is approximately true once the lower detection limit of the camera is passed, after  $\sim 1$  mm (Fig. S5.2). However, the distribution of side views shows an excess in the size range 2 to 3.5 mm. This is likely due to the fact that telling that a copepod is viewed from the top/bottom can be determined from the geometry of its antennae relative to its body, no matter its size; making sure that a copepod is viewed from the side requires additional details, which are easier to assess on larger individuals, inducing a bias in the manual selection of images. As explained in the main text, this has little consequence on the estimation of the distribution of the semi-axes ratios ( $r_2/r_1$  and  $r_3/r_1$ ) but does now allow the estimation of the distribution of  $r_1$  from these samples only.

## S6 Sensitivity of the correction factors to shape and orientation

### S6.1 Shape

In our dataset, the distribution of semi axes ratios was unimodal (see Fig. 4). Nevertheless, the proposed method can accommodate any distribution thanks to the use of the KDE approach (Parzen, 1962; Scott, 1979). Thus, it is interesting to verify how the correction factors vary in a multimodal scenario, for example when two populations of copepods with different shapes are present. Figure S6.1 shows some examples of synthetic PDFs of  $r_3/r_1$  for a mixture of two body shape distributions with varying proportions, and the effect on the correction factors, the other distributions ( $r_2/r_1$  and body orientation) being fixed. The top-left panel represents organisms with a round cross-section, that is to say  $r_3 \sim r_2$  (i.e. calanoid-like). Therefore, we used the same distributions for  $r_3/r_1$  and  $r_2/r_1$ : a Normal law with mean 0.41 and variance 0.0076 (values based on the fit to the UVP5 data). The second distribution represents organisms with a flatter cross-section i.e.  $r_3 \ll r_2$  (i.e. harpacticoid-like). We used a Beta distribution of parameters  $a = 2$  and  $b = 15$ . The parameter  $\alpha \in [0, 1]$  determines the proportions of samples from the two populations ( $\alpha = 0$ : 100% of the samples are from the first population;  $\alpha = 1$ : 100% are from the second one). The computed correction factors increase with  $\alpha$ , i.e. as the proportion of flatter organisms increases. This is to be expected since it is for this kind of shape that the viewing angle has the most consequences on the appearance of the organism. This illustrates that the correction factors strongly depend on community composition (and therefore on a correct modeling of the data). In particular, the correction factors obtained in the paper for the global UVP5 dataset should not be used blindly on other datasets. Instead, the required PDFs should be estimated from the data.

### S6.2 Orientation

In our simulations, the orientation of copepods relative to the camera was considered uniformly random. Nevertheless, with other imaging instruments, the orientation may be more constrained (e.g. with scanners like the ZooScan or in-flow imagers such as the FlowCam). It is possible to relax the uniformity assumption and verify how the correction factors vary with different degrees of constraint on the orientation.

Rotation can be performed around the x-axis of the copepod/ellipsoid

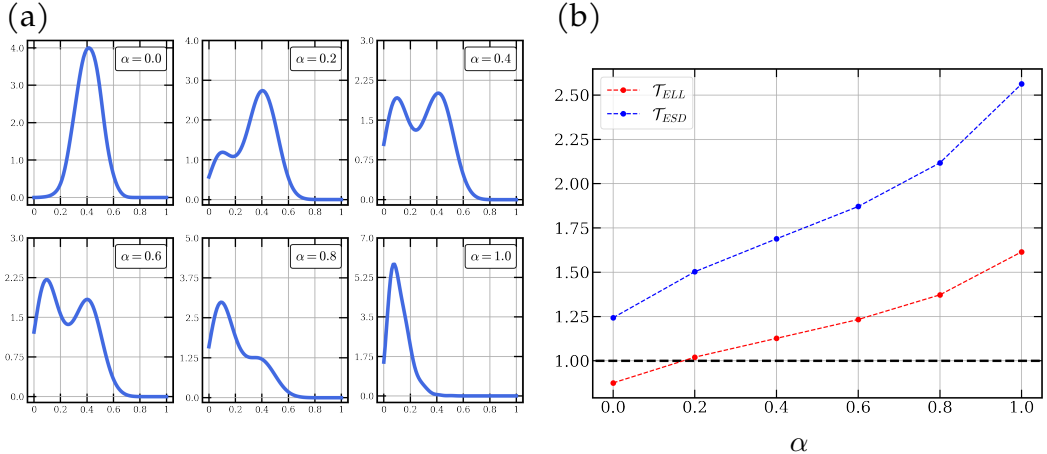


**Figure S6.1:** (a) Distribution of  $r_3/r_1$  for various mixtures of two subpopulations, from  $\alpha = 0$  (Normal distribution fitted on the  $r_2/r_1$  data of the UVP5 experiment), to  $\alpha = 1$ , Beta distribution with parameters  $a = 2$  and  $b = 15$ . (b) The corresponding correction factors for  $N = 10^6$  ellipsoids. The black dashed line indicates a correction factor of one, i.e. no error.

(i.e. the length) and determines whether we get a dorsal, side or ventral view (or something in-between); along the y-axis (i.e. the width) and, in the case of the UVP, this changes the vertical tilt of the organism; and along the z-axis, normal to the view plane, which, in the case of the UVP, changes the “cardinal” orientation of the organism. In the simulations, rotation along the z-axis is set to the identity (i.e. no rotation) since this does not influence the results at all; the x-axis rotation is free and uniform in  $[0, \pi]$  (so that  $\rho_2 \in [r_3, r_2]$ ); and the y-axis rotation is uniform in the interval  $[0, \theta_{\max}]$ : the higher  $\theta_{\max}$ , the more the ellipsoid can rotate vertically. Figure S6.2 shows the correction factors obtained. When  $\theta_{\max} = 0$ , all copepods are aligned on a plane (a “Zooscan-like” scenario). When  $\theta_{\max} = \pi/2$ , the results are the same as with a random uniform distribution. It is interesting to note that: (i) the correction factor for the  $\mathcal{M}_{\text{ELL}}$  method is relatively stable, while it varies more significantly for the  $\mathcal{M}_{\text{ESD}}$  method; (ii) the variation among the different orientation scenarii is much lower than for the different shapes (Figure S6.1).

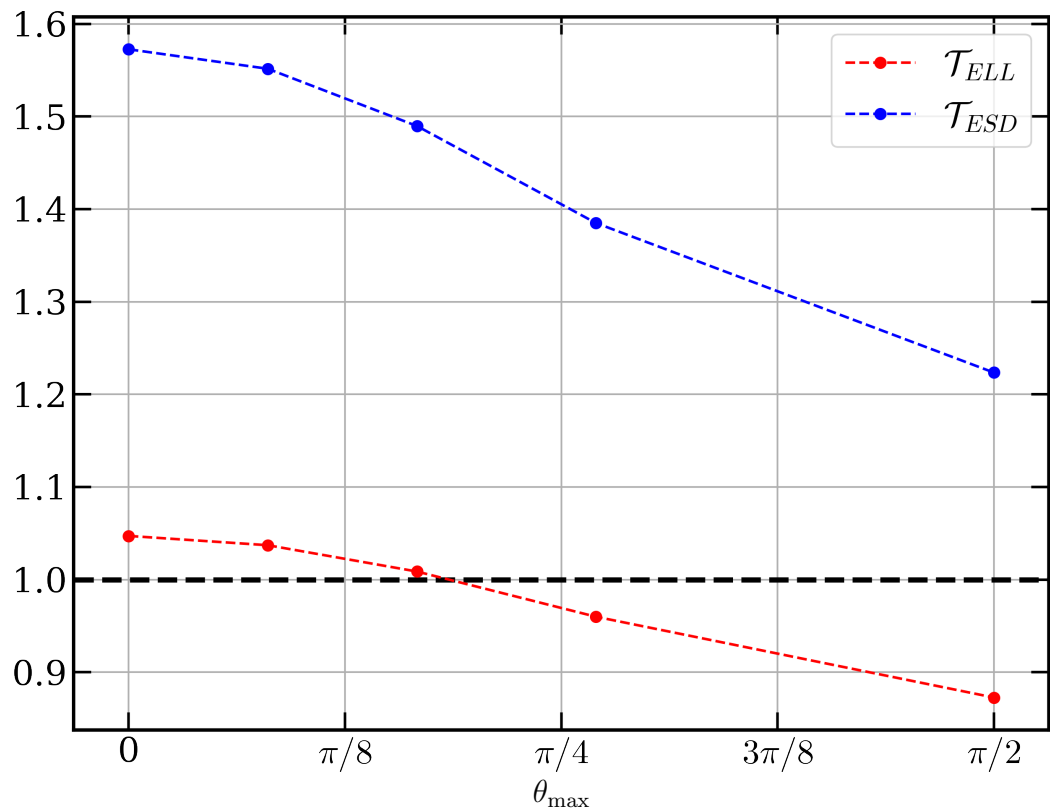
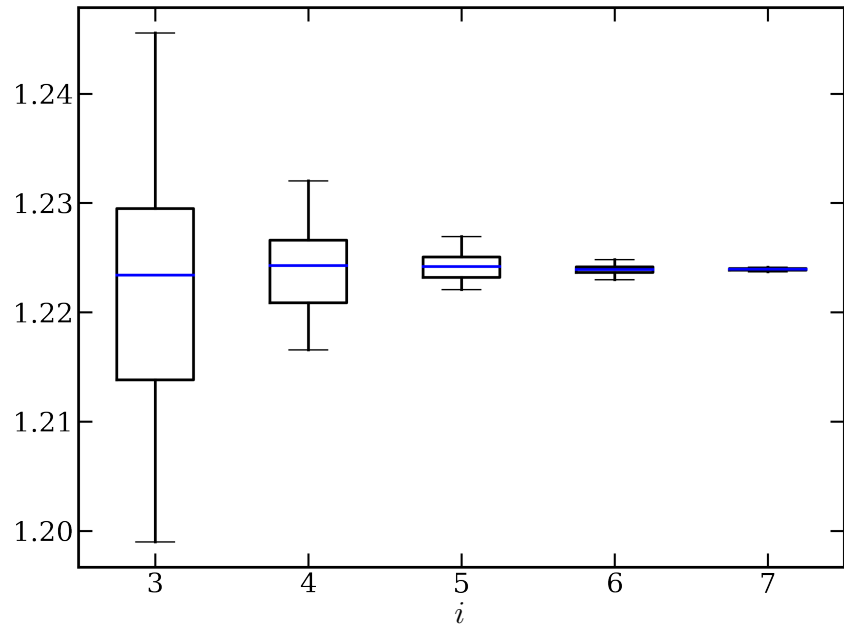


**Figure S6.2:** Evolution of the correction factors for varying ranges of allowed vertical rotation. The rotation angle around the y-axis,  $\theta$ , is restricted to the interval  $[0, \theta_{\max}]$ . Each dot of the plots corresponds to a simulation for a particular  $\theta_{\max}$ . The black dashed line indicates a correction factor of one, i.e. no error.

## S7 Sensitivity of the correction factors to the number of simulated ellipsoids

The number  $N$  of ellipsoids generated in the simulation only determines the precision of the estimation of those factors. As a matter of fact, the estimation of the correction factors tends to be perfect when  $N$  tends towards infinity. So this number has no reason to be related to the size of the dataset. Yet, it is still interesting to get an idea of the influence of  $N$  on the variance of the computed factors. Thus, we performed simulations with various numbers of ellipsoids  $N_i = 10^i, i \in \{3, 4, 5, 6, 7\}$ , lower than  $N = 10^8$  used in the paper. Fig. S7.1 shows that the variance of the correction factors becomes negligible for  $N_i \geq 10^6$ .

(a)



(b)

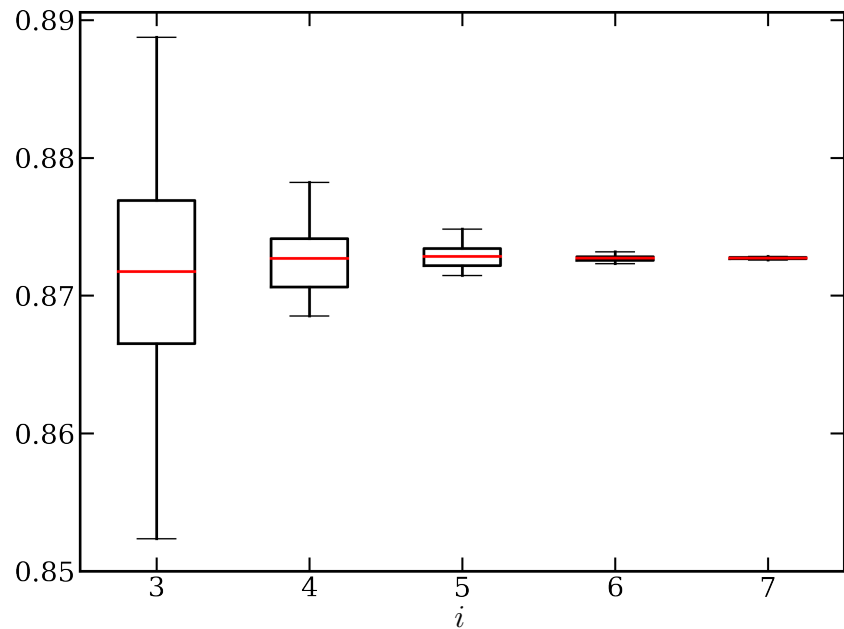


**Figure S7.1:** Corrections factors ((a)  $\mathcal{M}_{\text{ESD}}$ , (b)  $\mathcal{M}_{\text{ELL}}$ ) for  $N_i = 10^i$ ,  $i \in \{3, 4, 5, 6, 7\}$ . For each  $i$ , we computed the correction factors 50 times. The blue (red) line is the mean factor for the  $\mathcal{M}_{\text{ESD}}$  ( $\mathcal{M}_{\text{ELL}}$ ) method. The boxes and whiskers are drawn according to Tukey's definition (McGill et al., 1978).